MIT Libraries | DSpace@MIT

MIT Open Access Articles

The structure and composition of olivine grain boundaries: 40 years of studies, status and current developments

The MIT Faculty has made this article openly available. ***Please share*** how this access benefits you. Your story matters.

As Published: https://doi.org/10.1007/s00269-017-0935-9

Publisher: Springer Berlin Heidelberg

Persistent URL: https://hdl.handle.net/1721.1/131559

Version: Author's final manuscript: final author's manuscript post peer review, without publisher's formatting or copy editing

Terms of Use: Article is made available in accordance with the publisher's policy and may be subject to US copyright law. Please refer to the publisher's site for terms of use.

Massachusetts Institute of Technology

Physics and chemistry of minerals 40 anniversary manuscript No.
(will be inserted by the editor)

The Structure and Composition of Olivine Grain Boundaries:

40 years of studies, status and current developments

K. Marquardt · U. H. Faul

Received: date / Accepted: date

Abstract Interfaces in rocks, especially grain boundaries in olivine dominated rocks, have been subject to about 40 years of studies. The grain boundary structure to property relation is fundamental to understand the diverging properties of polycrystalline samples compared to those of single crystals. The number of direct structural observations is small, i.e. in range of 100 micrographs, and the number of measurements of properties directly linked to structural observations is even smaller. Bulk aggregate properties, such as seismic attenuation and electrical conductivity are sensitive to grain size, and seem to show influences by grain boundary character distributions. We review previous studies on grain boundary structure and composition and plausible relations to bulk properties. Experimentally determined seismic properties and rheology of olivine are sensitive to grain boundary characteristics. The grain boundary geometry is described using five independent parameters, generally their structural width is ranges between 0.4-1.2 nm and

Katharina Marquardt
Bayerisches Geoinstitut, Universität Bayreuth, 95447 Bayreuth, Deutschland
Tel.: +49(0)921/55-3846
E-mail: Katharina.Marquardt@uni-bayreuth.de

Ulrich Faul
Department of Earth, Atmospheric and Planetary sciences, Massachusetts institute of technology, 77 Massachusetts avenue, 53-918, Cambridge, MA 02139, USA
Research School of Earth Sciences, Australian National University, Canberra, Australia of U. Faul

the commonly used 1 nm seems a good approximation. This region of enhanced disorder is often enriched in elements that are incompatible in the perfect crystal lattice. The chemical composition of grain boundaries depends on the bulk composition. We determined the 5 parameter grain boundary character distribution (GBCD) for polycrystaline Fo_{90} and studied structure and chemistry at the nm-scale to extend previous measurements. Grain boundary planes close to perpendicular to the crystallographic c-direction dominate the grain boundary network. We conclude that linking grain boundary structure in its full geometric parameter space to variations of bulk rock properties is now possible by GBCD determination using EBSD mapping and statistical analyses.

Keywords Olivine · Grain Boundaries · upper mantle · deformation · seismic attenuation · electrical conductivity · forsterite · interfaces · segregation · incompatible elements

1 Introduction

Interfaces in rocks, especially grain boundaries in olivine dominated rocks, have been subject to nearly 40 years of studies. One of the first authors who noted the importance of relating structure to property in further research on the nature and role of grain boundaries was McClay (1977) while reviewing pressure solution and Coble creep in rocks and minerals. 40 years later the grain boundary structure to bulk rock property relation is still being debated. This contribution is an attempt to review past work and while refraining to claim completeness, we hope to indicate open questions and trigger new studies using newly available methods. Developments with and observations on crystallographically and chemically simpler systems such as ceramics, with relevance for the Earth (e.g. MgO) allow identification of structure-property relations directly.

Olivine incorporates a broad range of elements in traces at ppm and ppb level (e.g. Garrido et al., 2000; Davies et al., 2006; Lee et al., 2007; Drouin et al., 2009; De Hoog et al., 2010; Foley et al., 2011, 2013), including transition metals with variable valance states. Therefore, the structure-property relations are best identified on simplified systems with high density (e.g. derived from solgel-processes, from oxides or from nano-sized precursors). With respect to diffusional properties the most important element controlling the defect chemistry at given pressure, temperature, oxygen fugacity and silicon activity was shown to be iron (Chakraborty et al., 1994; Chakraborty, 1997; Petry et al., 2004). This led to the conclusion that any diffusion related properties measured on iron free systems cannot be used to model these properties in natural systems. We present some new observations and highlight recent developments that offer new possibilities for gaining a more complete understanding of grain boundaries. While the examples given for the terminology in the appendix are of general character, and therefore include observations from ceramics, the main part of this contribution will focus on interfaces in olivine dominated rocks. In cases where we report results from the *ceramics literature we will mark it in cursive.*

Rocks are polycrystalline materials (Lloyd et al., 1997), thus individual crystals joint to each other by a three-dimensional network of internal interfaces − the grain boundary network (Rohrer, 2011b). The principal characteristics of the texture of a 'monomineralic' rock is the relative areas of different types of grain boundaries and the way that they are connected. Such a description intrinsically includes information on aspect ratio, lattice preferred orientation, relative orientation of neighboring grains (disorientation, to be defined later) but excludes grain size variations.

Single crystal properties (e.g. Durham and Goetze, 1977; Durham et al., 1977) are markedly different from bulk rock properties (e.g. Phakey et al., 1972; Goetze et al., 1973; Poirier, 1985; Karato et al., 1986; Marquardt et al., 2011a,b; Kohlstedt and Hansen, 2015). Grain boundaries significantly influence a number of the physical properties of rocks (e.g. Wenk, 1985). Their presence influences creep strength in diffusion creep (e.g. Cooper and Kohlstedt, 1984; Hirth and Kohlstedt, 1995; Sundberg and Cooper, 2008; Hansen et al., 2011, 2012a,c,b). Grain boundary diffusion is orders of magnitude faster compared to volume diffusion in olivine include (for example Farver et al., 1994; Farver and Yund, 2000; Milke et al., 2001, 2007; Hayden and Watson, 2008; Dohmen and Milke, 2010; Demouchy, 2010; Marquardt et al., 2011c,d; Gardés et al., 2012). Furthermore, seismic properties are directly influenced by grain boundaries as evidenced by a marked grain size effect found by Jackson et al. (2002, 2004). Electrical conductivity has also been found to be grain size sensitive (ten Grotenhuis et al., 2004, 2005; Dai et al., 2008; Farla et al., 2010; Laumonier et al., 2017). However, some studies conclude opposingly that grain boundaries have no effect on electrical conductivity (Roberts and Tyburczy, 1991). Variable grain boundary energy influences the melt distribution and thus indirectly influence bulk properties, which has been proposed by Anderson and Sammis (1970) and Solomon (1972). First experiments with respect to melt networks at olivine interfaces where conducted by Waff and Bulau (1979).

Despite their importance, and despite the amount of studies general relations between olivine grain boundary structure and associated properties are still poorly understood, but are *extensively evident in ceramics* (summarising works include Sutton and Balluffi, 1995; Rohrer, 2007; Harmer, 2010; Rohrer, 2011a, 2015). Structure property relations have been established using the grain boundary geometry in its full five parameter space: the grain boundary character distribution (GBCD). *The key geometrical information directly related to bulk properties appears to be the grain boundary plane distribution (GBPD); it is proportional to the inverse of grain boundary energy distribution (GBPD* $\propto$ *1/GBED, (Olmsted et al., 2009; Rohrer, 2011b; Holm et al., 2011; Bean and McKenna, 2016)). Rohrer (2007) further summarises that: 'Grain boundary plane distributions in polycrystals are anisotropic and scale invariant during normal grain growth. This suggests that the GBCD is an intrinsic characteristic of the microstructure. The most common grain boundary planes are those with low surface energies and the grain boundary populations are inversely correlated with the grain boundary energy. These observations indicate that the GBCD develops deterministically based on the relative energies of the boundaries and can be influenced by altering these energies.'.*

Furthermore, the volume of the grain boundary region is linked to the GBPD through its positive correlation with grain boundary energy (e.g. Olmsted et al., 2009; Holm et al., 2011; Bean and McKenna, 2016). It is observed that the GBPD sensitively changes with varying grain boundary composition (Cho et al., 1999; Pang and Wynblatt, 2006), which is explained as a result of changing grain boundary energies(Pang and Wynblatt, 2006; Holm et al., 2011). Consequently the structure of grain boundaries varies with composition, which can thus be regarded as a sixth independent parameter that affects the 5 parameter space.

Moreover, a positive correlation between grain boundary volume and grain boundary diffusion has been observed in molecular dynamic simulations in forsterite (Adjaoud et al., 2012; Wagner et al., 2016) as well as in *many computational studies in ceramics (Olmsted et al., 2009; Holm et al., 2011; Bean and McKenna, 2016).* The

GBPD may therefore, in a first approximation, be linked to the grain boundary volume, energy, viscosity and diffusivity and a true structure to property relations can be established. In this contribution we review past work on grain boundaries, show new data on the composition and structure of grain boundaries and conclude that quantitative information that encompasses the full 5-6 parameter space can be obtained by using the GBCD and GBPD.

1.1 Grain boundary geometry

The term grain boundary defines the interface where two minerals of the same phase are in contact (Figure 1). The only characteristic that varies between the two grains (crystals) is the orientation of the crystal lattice. In the green grain a small angle grain boundary intersects the high angle grain boundary of the red grain. The inequality of the dihedral angles is indicative of the lower energy of the small angle grain boundary (sub grain boundary) which has been used to infer the relative energies of low angle grain boundaries (Duyster and Stöckhert, 2001).

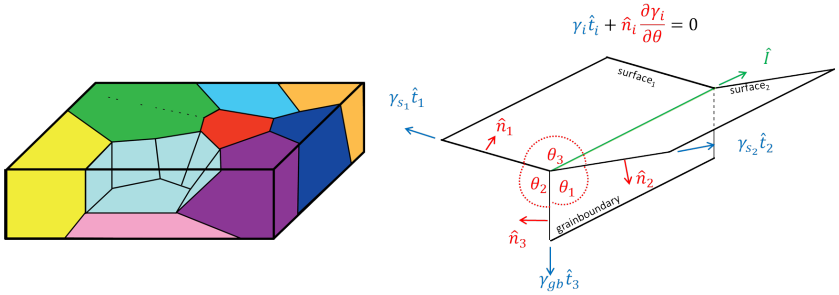

Fig. 1 The left side shows a schematic illustration of a polycrystalline sample where all grains have different crystallographic orientations, but are of the same phase (drawn after an initial sketch by Gregory S. Rohrer). On the right the Herring equation with an illustrative sketch is shown. In this form θ indicates the dihedral angles. The inclination of the individual grain boundaries is given by ψ and not indicated in the scheme. γ_i is the excess free energy of the i^{th} boundary (surface=s, grain boundary=gb), $\hat{n}_i$ is the unit boundary normal of the i^{th} boundary and perpendicular to the triple line, $\hat{I} = \hat{n}_i \oplus \hat{t}_i$ which is common to all tree adjacent boundaries. ψ_i is defined as the right handed angle of rotation about $\hat{I}$ of the i^{th} boundary from a reference direction. The derivative terms are referred to as torque terms, $\hat{t}_i$ and reflect the dependence of interface energy on orientation about the triple junctions at fixed $\hat{I}$ (e.g. Adams et al., 1999; Rollett and Rohrer, 2017).

The grain boundary geometry is given using five macroscopic degrees of freedom (e.g. Mishin and Herzig, 1999; Rollett and Rohrer, 2017), this is visualised in Figure 2. The misorientation between two adjacent crystals is described using three Eulerian angles that are given with respect to one of the adjacent crystal lattices, conventionally: σ_1, ϕ, σ_2 (e.g. Wenk, 1985). The grain boundary plane is described using the two remaining degrees of freedom with one radial and one azimuthal angle: Φ and θ (Engler and Randle, 2009; Rollett and Rohrer, 2017). This description encompasses all types of grain boundaries: low angle grain boundaries, high angle grain boundaries of general and special character, where special generally refers to either geometrically or from a property point of view special (Randle and Davies, 2002).

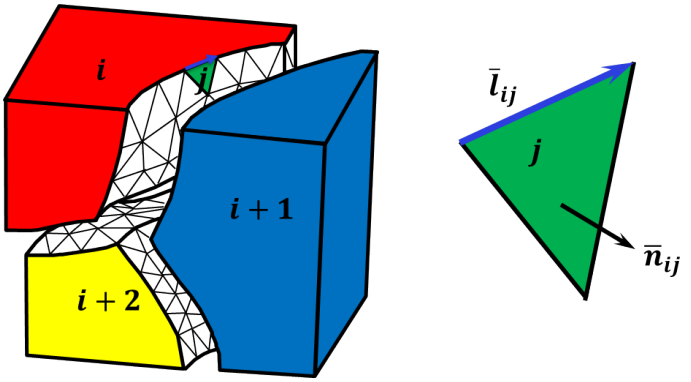

Fig. 2 Schematic illustration of a 3D polycrystalline sample, where the full 5 parameters needed for the macroscopic description of the grain boundary geometry are given. Figure is varied from the sketch in the publication (Rohrer, 2007).

Low angle grain boundaries are build from periodically spaced dislocations. The small angle grain boundary has the misorientation angle, θ across the boundary. For small misorientations this can be approximated using the burgess vector $\bar{b}$ of the dislocation and their spacing h as

$$\theta = \bar{b}/h \tag{1}$$

The low angle tilt grain boundary misorientaion can be related to the grain boundary energy (Read and Schockley, 1950):

$$E_{\text{tilt}} = \frac{Gb^2}{4\pi(1-\nu)} * \frac{\theta}{b} * (A - ln\theta) \tag{2}$$

where ν is the Poisson's ration and A the elastic strain energy resulting from the lattice distortions around the dislocation cores, and G the shear modulus. Such distortions around individual dislocations forming low angle grain boundaries have been mapped using TEM (Johnson et al., 2004). TEM investigations on low angle grain boundaries date back to at least (Phakey et al., 1972; Goetze et al., 1973; Durham et al., 1977; Durham and Goetze, 1977). Modern TEM methods allow to obtain full 3D data on dislocations by tomography (Mussi et al., 2014). This formulation applies to low angle grain boundaries. It is not applicable to high angle grain boundaries, because as soon as the cores of the dislocations overlap, we cannot distinguish individual dislocations anymore. This misorientation defines the onset of large angle grain boundaries. Heinemann et al. (2005) observed that this transition occurs above 20° misorientation in forsterite. A relation to the larger lattice parameters in silicates, in comparison to metals was speculated to be the cause. They showed that the Read and Schockley (1950) model is well applicable even thought the initial approximations are derived for cubic crystal system. This was further supported by molecular dynamic simulation studies by Adjaoud et al. (2012) and Wagner et al. (2016). For small angle twist grain boundaries a similar treatment is suitable (Read and Schockley, 1950).

High angle grain boundaries used to be described using geometrical models. The coincidence side lattice (CSL) model yields the three-dimensional lattice coincidence (Chan and Balluffi, 1986; Sutton and Balluffi, 1995). The Σ value gives the inverse of the coincidence site density at the grain boundary plane (Vonlanthen and Grobety, 2008) such that an actual physical meaning of the CSL theory could be obtained. In principle all planar grain boundaries must be periodic - because they are interfaces between two periodic crystals. However, the past two decades

of grain boundary studies in ceramics show that the Σ notation has no significant meaning besides its short-hand notation, furthermore these so called 'special' grain boundaries are not particularly common in polycrystals (e.g. Saylor et al., 2003, 2004; Vonlanthen and Grobety, 2008; Rohrer, 2007) a situation referred to as the 'Sigma enigma' (Randle and Davies, 2002). Also in olivine, Marquardt et al. (2015) found no preference for special (low Σ CSL) grain boundaries of any type, which is probably enhanced by the relatively low symmetry of olivine. Therefore we will not further consider this model in this overview.

Of all the relations between the geometry of high angle grain boundaries and their properties the most fundamental relation is that of geometry to grain boundary energy, γ. If we consider only interfacial energies, the vector ($mathbfb$) sum of the forces must be zero in equilibrium:

$$\gamma_1 \mathbf{b}_1 + \gamma_2 \mathbf{b}_2 + \gamma_3 \mathbf{b}_3 = 0 \tag{3}$$

If we rearrange equation 3 we obtain the Young equation (sine law):

$$\frac{\gamma_1}{\sin\theta_1} = \frac{\gamma_2}{\sin\theta_2} = \frac{\gamma_3}{\sin\theta_3} \tag{4}$$

If the energies of the three interfaces are known, the dihedral angles can be computed. However this is only viable for isotropic systems (for example soap bubbles) - for anisotropic systems, thus all crystals, the torque terms - as illustrated in Figure 1 - have to be taken into account and the full Herring equation (eqn. 5) is appropriate for usage (its reduction yields again the Young equation):

$$\gamma_i \hat{t}_i + \hat{n}_i \frac{\partial \gamma_i}{\partial \theta} = 0 \tag{5}$$

In polycrystalline samples Marquardt et al. (2015) observations indicate that

grain boundary energy minimisation is controlled by surface energy reduction of the individual grains in contact and not by adapting the grain boundary plane orientation of special atomic configuration across the interface. This is in agreement with many studies on ceramics (Saylor, 2001; Sano et al., 2003; Saylor et al., 2004; Sano et al., 2005; Pang and Wynblatt, 2006; Dillon et al., 2010). Thus the ideal shape or minimum surface energy of each crystal in a polycrystal depends on the material the individual crystal is in contact with, e.g. another crystal, melt, fluid, or segregated elements.

1.1.1 The five parameter grain boundary character distribution (GBCD)

The GBCD is sometimes referred to as interface character distribution (ICD, Fang et al., 2016) used to be reduced to one or three parameters. The disorientation angle, which is one single parameter which is in geological literature often also called misorientation here. We will use disorientation here, Figure 5a. The axis and angle of disorientation (e.g. Lloyd et al., 1997; Fliervoet et al., 1999) includes three parameters (Figure 5b). These simplifications were necessary, because the full geometrical parameter space discretised in for example steps as large as 10° results in approx. $60 \cdot 10^3$ geometrically distinct grain boundaries in the orthorhombic crystal system (Rohrer, 2011b; Marquardt et al., 2015). This number increases for finer discretisation or lower crystal symmetries. Therefore, the numbers of previous grain boundary observations is small compared to real number of geometrically distinct grain boundaries.

The grain boundary plane distribution (GBPD) is part of the GBCD and given by the remaining two parameters. One radial and one azimuthal angle: Φ and θ, frequently displayed independently of misorientation as in (Figure 5c). The new developments in EBSD allow to statistically extract these two parameters. The anisotropic distribution of the grain boundary plane at a specific disorientation about a specific axis means, in other words that if the disorientation of two adjacent crystals is constant, particular grain boundary plane orientations are

more common than others and thus energetically favourable. In Figure 5d and 5e the grain boundary plane distributions represent the relative areas of different grain boundary planes at specific disorientation about specific axis, here 60° about [100] and 90° about [001]. The plots in c-d are stereographic projections. All data in Figure 5 are obtained from a solgel Fo_{90} sample, with minor amounts of Ti partitioned to the grain boundaries. The results will be discussed below and in full detail and in comparison to other GBCD in a following publication.

The number of published direct observations on grain boundaries amounts to about 100 transmission electron micrographs for olivine grain boundaries. Most observations stem from the works of Phakey et al. (1972); Goetze et al. (1973); Durham and Goetze (1977); Durham et al. (1977); Vaughan et al. (1982); Kohlstedt (1990); de Kloe (2001); Hiraga et al. (2002, 2003); Adjaoud et al. (2012); Burnard et al. (2015) and the various studies of the ANU group (Faul et al., 1994; Drury and Fitz Gerald, 1996; Cmíral et al., 1998; Faul, 2000; Jackson et al., 2004; Faul et al., 2004) as well as from the study of Fei et al. (2016).

It should be noted that recent development of high-speed electron backscatter diffraction (EBSD) mapping now allows for characterisation of large numbers of grain boundaries in their five parameter space (four parameters from 2D sections and the fifth calculated using stereology, or directly five by serial sectioning). The number of grain boundaries characterised using EBSD amount to $10^4, 10^5$ in individual studies (e.g. Adams et al., 1993; Zaefferer and Wright, 2009; Marquardt et al., 2015).

1.1.2 New techniques to measure the full five parameter space of grain boundaries

The study of grain boundaries in polycrystals went through a drastic change since the availability of automated EBSD mapping, which allows to sample the immense parameter space of the grain boundary character. EBSD techniques are well described in several text books (e.g. Maitland and Sitzman, 2007; Zaefferer and Wright, 2009; Engler and Randle, 2009; Rollett and Rohrer, 2017) and efficient

overviews are given in (e.g. Rohrer, 2011b). To measure the GBCD two main approaches have been used. 3D serial sectioning and stereological analyses of two-dimensional orientation maps (Randle and Davies, 2002; Rohrer et al., 2004). Stereology is, while being much simpler than sectioning, only applicable to materials without significant orientation texture or lattice preferred orientation (LPO). The stereological concept has been applied to many different materials many comparisons of different research groups to 3D sectioning proved its applicability (e.g. Adams et al., 1993; Randle and Davies, 2002; Kim et al., 2006; Reed et al., 2012).

1.2 Grain boundary energy, structure and width

The grain boundary structure is changing on the atomic scale to minimise the respective surface energies, resulting in different grain boundary geometries. The grain boundary structure can be studied at the nm-scale using HRTEM in combination with electron exit wave reconstruction (e.g. Adjaoud et al., 2012). True atomically resolved micrographs of olivine grain boundaries have not been published as yet. It should be noted that the observed grain boundary structure of not perfectly straight grain boundaries varies on the scale of less than 100 nm, visible in HRTEM micrographs. Thus every few tens to hundreds of nm we can define a new grain boundary structure. Steps and facets on grain boundaries are necessary to accommodate a particular grain boundary plane orientation. Instead of straight facets grain boundaries are also observed to be curved in two orthogonal dimensions, again facilitated by unit cell sized steps. The unit cell criterion arises because we require charge neutrality and it has been observed in evaporation experiments, that no leaching layer forms - thus evaporation occurs in stoichiometric ratios. But roughness and steps may also arise from dislocations or sub-grain boundaries intersecting the grain boundary can cause steps.

Because the atoms at grain boundaries are less ordered relative to the olivine crystal interior but more influenced by the close proximity of the adjacent crystals they are more ordered than pure melt. This is reflected in the faster diffusion along

grain boundaries compared to the crystal volume, and slower diffusion than that in melt. Furthermore, grain boundaries show higher viscosity than melt. Molecular dynamic simulations inferred a relation of diffusivity and viscosity to surface energy (e.g. Gurmani et al., 2011) and crystal orientations with higher surface energy show lower self-diffusion coefficients of all ionic species. The relation between viscosity, diffusion and self diffusion for ionic liquids is simple and given by the Nerst-Einstein equation, it is discussed by Avramov (2009). However, it is not applicable to silicate melts as they are non-ionic-liquids. Other approaches to obtain the grain boundary viscosity from molecular dynamic simulations can be obtained from the Green-Kubo relation expressing the viscosity as function of the stress tensor time correlation function as exploited by Mantisi et al. (2017). Note that the surface energies given in Gurmani et al. (2011) where calculated in contact with vacuum rather than in contact with melt and are very similar to the energies calculated by Watson et al. (1997). Other simulation methods yield varying surface energies, also affected by the contact medium (de Leeuw et al., 2000a,b; King et al., 2010; Bruno et al., 2014, 2016).

In the following we review and examine the structural width and the effective width of grain boundaries in experimentally produced polycrystalline olivine aggregates of samples of different origin and composition. We summarise previous findings, the terminology and end with the observation that the width of grain boundaries remains a parameter to be determined.

The width of grain boundaries, δ, is subjected to debates for several decades. Generally it appears that it is necessary to distinguish the structural (or physical) grain boundary width, δ_{struc} defined as the distance between two adjacent crystal lattices and the effective grain boundary width, δ_{eff}, which is the width active to enhance a specific process occurring at the grain boundary. The effective width may be different for different processes and is an empirical parameter used in the absence of physically observable differences.

The structural grain boundary width, δ_{struc} is defined as the distance between two adjacent perfect crystal lattices. While some studies find that the lattice planes of neighbouring crystals are directly in contact, they abut, without an intervening disordered region (Kohlstedt, 1990; Hiraga et al., 2002; Vaughan et al., 1982), others find a disordered region between the two adjacent crystal lattices with a width of about 1 nm (Drury and Fitz Gerald, 1996; Tan et al., 2001; Faul et al., 2004). As both results are obtained from imaging they both yield the structural width. The structural width of low-angle grain boundaries has been determined by Ricoult and Kohlstedt (1983) to be three to four times smaller than the dislocation spacing and approx. in the range of 5-8 nm. Furthermore, the importance of hydrated grain boundaries was greatly emphasised for tectonites, including quartz and peridotite mylonites (e.g. White and White, 1981). They observe that a grain boundary region of 10 - 30 nm is more susceptible to electron beam damage compared to the crystal interior and conclude, that this region has generally different properties caused by presence of a fluid and/or a highly distorted crystal structure layer. White and White (1981) suggest that the grain boundary width of olivine grain boundaries is orientation dependent. For hydrated grain boundaries in halides width of up to 2 μm where discussed (Mistler and Coble, 1974).

The effective grain boundary width, δ_{eff}, in contrast is defined as the zone around a grain boundary where a specific process is enhanced. The effective grain boundary width may be orders of magnitude larger compared to the structural width, and may not be directly observed using SEM; in TEM δ_{eff}, if caused by lattice distortions, may be imaged using geometrical phase analyses as exemplified on low angle grain boundaries in olivine by Johnson et al. (2004). It has been observed that element segregation (max. 7 nm Hiraga et al., 2002) and diffusion along a grain boundary can occur at an effectively larger region; this was attributed to lattice strain and/or a *space charge layers associated with grain boundaries in ionic crystals (e.g. Kliewer and Koehler, 1965; Cinibulk et al., 1993; Kleebe, 2002).*

Such strained and/or charged layers allow for variations in polaron conduction or element diffusion rates. Determining the effective grain boundary width, δ_{eff}, during deformation or diffusion from the respective formulas results in width estimates ranging from approx. 1 nm to regions as wide as several μm (e.g. Mistler and Coble, 1974; Hirth and Kohlstedt, 2003; Marquardt et al., 2011d; Hashim, 2016). Constituting equations for diffusional or rheological processes include the effective grain boundary width, as an imperative parameter (Farver et al., 1994; Kaur et al., 1995; Dillon and Harmer, 2007).

The effective grain boundary width and the width of the region elements partition to (segregated) are affected by: (1) lattice misfit of the adjacent grains, (2) misfit lattice strain due to the difference between the size of a solute ion and that of the ideal strain-free lattice site (Hiraga and Kohlstedt, 2007; Hiraga et al., 2007; Marquardt et al., 2011d; Lejcek, 2010), and (3) in ionic crystals a space charge layer can be present (e.g. Lehovec, 1953; Kliewer and Koehler, 1965; Kingery, 1974). These effects can be visualised for example by depicting the displacement of atoms with respect to the place they would occupy in a perfect crystal lattice, examples have been calculated with molecular dynamic simulations (e.g. Ghosh and Karki, 2014; Wagner et al., 2016; Mantisi et al., 2017). Furthermore, the effective width of element diffusion of a specific element along a specific interface might be as large as 10-30 nm (Mistler and Coble, 1974; Marquardt et al., 2011d). Enhanced diffusion around a grain boundary was already discussed by White and White (1981). In contrast, Farver et al. (1994) high-lighted that the average effective grain boundary width for Mg grain boundary diffusion in forsterite is in good agreement with the structural grain boundary width determined from HRTEM micrographs, which is in the range of 1 nm.

Concepts to explain these large variations where suggested by Peterson (1983), who stated that the values for δ_{eff} that are obtained thought diffusion studies are too large depending on whether or not grain boundary diffusion occurs parallel or perpendicular to the grain boundary. Where diffusion is parallel to the grain

boundary, ($D^{\parallel}_{gb}$) the process depends on $D_{gb}\delta$, or where diffusion occurs across the grain boundary $D^{\perp}_{gb}$ the process depends on $D^{\perp}_{gb}\delta^{-1}$ e.g. grain boundary migration. Therefore, Peterson (1983) concluded that even thought direct observations are easily interpreted, kinetic techniques may be more appropriate for the interpretation of the various grain boundary widths. Furthermore, Ricoult and Kohlstedt (1983) suggested that impurities will significantly slow down grain boundary migration ($D^{\perp}_{gb}\delta^{-1}$) and will have little effect on grain boundary diffusion ($D^{\parallel}_{gb}$).

This last statement seems to become more unlikely based on the growing body on grain boundary diffusion studies in ceramics and metals that rather suggest that both, grain boundary migration and grain boundary diffusion can increase or decrease with different types of impurities that segregated to grain boundaries (e.g. Ching and Xu, 1999; Cho et al., 1999; Dillon and Harmer, 2007; Palmero et al., 2012; Raabe et al., 2014; Homer et al., 2015).

1.3 Grain boundary chemistry - partitioning/segregation to grain boundaries

It is now generally accepted that high angle grain boundaries are enriched in trace elements that are relatively *incompatible* in the crystal interiors (e.g. Tan et al., 2001; Hiraga et al., 2002, 2003, 2004; Faul et al., 2004). Drury and Fitz Gerald (1996) were the first to measure grain boundary compositions in olivine but in relation to melt films. Some early studies found no enrichment at grain boundaries (Kohlstedt, 1990), this was later explained as related to the substantial capability increase in transmission electron microscopic methods that took place during these years. De Kloe et al. (2000) pointed out that the absence of a compositional difference between intra- and inter granular areas might related to the positioning difficulties of a condensed beam, which could further cause irradiation damage.

The enrichment of trace elements at high angle grain boundaries is a result of segregation (partitioning), where elements that do not fit into the structure of the adjacent crystals partition/segregate to the grain boundary (Hiraga et al., 2002; Faul et al., 2004; Hiraga and Kohlstedt, 2007; Hiraga et al., 2007), a process

analogous to element partitioning between melt and crystal (and similarly inferred to be temperature and pressure dependent). Grain boundaries may thus serve as a container for incompatible elements in the Earth's interior (Hiraga et al., 2004; Sommer et al., 2008). However, Eggins et al. (1998) show in their ICP-MS and microbeam (EMP, LA-ICP-MS) study on peridotites that all trace element content can be accounted for without accessory minerals or grain boundaries for grain sizes above μm-sizes. An exception might be noble gases; solubility experiments for He in olivine Parman et al. (2005) show measurable quantities of helium interpreted to be trapped between grains or adsorbed on grain boundaries.

The grain boundary energy is influenced through chemical segregation, where the grain boundary energy in most observations in *ceramics decreases, but occasionally increases; the latter results in creep resistance reduction (Yasuda et al., 2004; Raabe et al., 2014). In ceramics the prevailing consensus is that segregation influences grain boundary diffusivity, and in consequence bulk viscosity in diffusion creep*. It can be hypothesised that the creep resistance in rocks is influences through grain boundary segregation.

1.4 Pre-melting

Based on the observation that grain boundaries often have a different composition and are more disordered compared to grain interiors, the concept of 'pre-melting' has been proposed. Its occurrence was recently described for geological materials (Levine et al., 2016). *Pre-melting involves the formation of nanometer-scale intergranular films with liquid-like properties, such as static and dynamic disorder, below the bulk melting point (the same as surface or interface melting (Mott, 1951)). Consequently, diffusion rates within this region are higher than normal grain boundary diffusivities and approach those in a liquid (e.g. Kaplan et al., 2013). Material science melting studies in mono-mineralic substances of high purity, and on single crystals show that melting occurs along grain boundaries and grain surfaces below the actual bulk-melting temperature (Dash, 1999; Alsayed et al., 2005; Mei and Lu, 2007;*

Han et al., 2010; Bhogireddy et al., 2014). Pre-melting can begin at temperatures of 90 % of the bulk melting temperature, as observed in simulations and studies of ceramics (Luo et al., 2005; Mellenthin et al., 2008; Luo and Chiang, 2008; Dillon et al., 2010).

Levine et al. (2016) summarised evidence for pre-melting and shows its existence in gneiss. This study summarises the causes for pre-melting at dislocations (also applicable to grain boundaries) as: 1) a lowering of the activation energy as a result of stored strain energy, 2) an increased abundance of weakened bonds located within sub grain boundaries, thus less energy is required to weaken the remaining bonds (Hartmann et al., 2008) , 3) enhanced diffusion rates along the sub grain boundaries and 4) a local lowering of the melting temperature due to 'water and water-derived species'.

Pre-melting is related to, but should not be confused with early partial melting (EPM) a process where point-defect condensation leads to small melt factions that are unusually enriched in SiO_2, not expected to occur in thermodynamic equilibrium. This has been described in the system olivine-pyroxene (e.g. Doukhan et al., 1993; Raterron et al., 1995, 1997) and Raterron et al. (2000) concluded that the process can be well-explained by sluggish point-defect equilibration using the model of Nakamura and Schmalzried (1983).

1.5 Melt distribution to study grain boundary energy

The distribution of the melt phase at the grain scale is a function of grain boundary energy (e.g. Bulau et al. (1979); Vaughan et al. (1982); Cooper and Kohlstedt (1982); Toramaru and Fujii (1986b,a); Wanamaker and Kohlstedt (1991) and Bagdassarov et al. (2000)). For example, while basaltic melt penetrates deeply into high angle olivine grain boundaries (a small dihedral angle), sub grain boundaries show a large dihedral angle, indicating their much lower grain boundary energy (Figure 4d in Cmíral et al. (1998); Duyster and Stöckhert (2001)). A static model is frequently used to determine the relative grain boundary energies by measuring

the dihedral angle at the contact of two grains with melt (Waff and Bulau, 1979; Bulau et al., 1979). In the case of a melt-bearing polycrystal, using the assumption of isotropic grain boundary energies, γ_{gb} and isotropic liquid-crystal energies, γ_{sl}, the Herring relations can be reduced to:

$$\cos\frac{\theta}{2} = \frac{\gamma_{gb}}{2\gamma_{sl}} \tag{6}$$

The dihedral angle is the angle enclosing the second phase, i.e. the melt. This is shown in Figure 3 and is a specific case of surface energy relations between the same crystal phases as displayed in Figure 1.

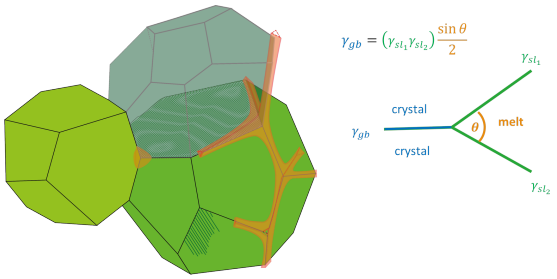

Fig. 3 Schematic illustration of a 3D isotropic polycrystalline sample, with two melts with different wetting properties, left non-wetting, right, wetting along triple junctions. No examples for wetted grain boundaries is given. It is important to remember that such illustrations are based on static hypothetic considerations. This does not account for dynamic reorganisation where wetted grain boundaries and melt pools at quadrupole junctions form transient features (e.g. Walte et al., 2005). Figure was inspired by a sketch in the PhD-thesis of Rene de Kloe (de Kloe, 2001).

Because of the simplicity of the dihedral angle measurements compared to interfacial energy determination, dihedral angles have been measured for a range of systems (an overview is given in Faul (2000); Laporte and Provost (2000); Bagdassarov et al. (2000)). Dihedral angles $> 0^\circ$ up to 60° yield interconnected melt without wetting grain boundaries in the isotropic theory. For dihedral angles $> 60^\circ$ the formation of an interconnected melt network requires increasing melt contents. The idealized isotropic model is self-similar, i.e. independent of grain

size. A grain size dependance of the melt distribution enters only in the models of Takei and Holtzman (2009b).

Instead of the true dihedral angle, which requires 3D observations (e.g. Cmíral et al., 1998), the distribution of the melt is frequently described using the distribution of apparent dihedral angles measured from 2D sections (e.g. Jurewicz and Jurewicz, 1986). This approach assumes isotropic surface energies; however, the surface energy anisotropy of olivine is non-negligible (e.g. Cooper and Kohlstedt, 1982; Watson et al., 1997; de Leeuw et al., 2000a; Faul et al., 2004; King et al., 2010; de Leeuw et al., 2010; Gurmani et al., 2011; Adjaoud et al., 2012).

Surface energies also depend on the composition of the melt as shown by Wanamaker and Kohlstedt (1991). Using the sessile drop technique (i.e. an additional liquid-vapour interface) they showed that the wetting angle (obtained from a variation of Herrings relations) increases with increasing silica content. Wanamaker and Kohlstedt (1991) conclude that the interfacial energy increases with increasing silica content, but for different Ca, Na, K containing silica melts and different crystallographic surfaces the relations become more complex. Similar to Wanamaker and Kohlstedt (1991), Schäfer and Foley (2002) used the sessile drop technique to study the variation of mineral-melt interfacial energy for the minerals olivine, enstatite, diopside, and spinel ad found that surface energy increases in that order. Finally it should be noted, that the grain boundary energy can be determined from grooved triple junctions of grain boundaries that arise from thermal etching or from internal triple junctions (e.g. Rohrer et al., 2004; Rohrer, 2011b).

The isotropic model together with melt fraction for the description of such solid-liquid systems is still a common procedure, despite the clear advantage of the description using contiguity as introduced by Takei (1998).

$$\varphi = \frac{2L_{\mathrm{ss}}}{L_{\mathrm{sl}} + 2L_{\mathrm{ss}}} \tag{7}$$

Contiguity is defined as the ratio between the length of solid-solid interfaces L_{ss} and the total grain boundary length. The factor 2 is a result of the two surfaces

that form the grain boundary. Note that the contiguity for anisotropic materials is a tensor which is by definition symmetric: $\varphi_{ij} = \varphi_{ij}$ (Takei, 1998). Contiguity (the contact area) can also be expressed as wetness, which is the inverse: $\psi = 1 - \varphi$.

Most early studies used relatively low resolution to measure the dihedral angle. However, the resolution is critical because thin layers on grain boundaries contribute disproportionally to wetness but little to melt fraction. For the system of olivine with a basaltic melt, dihedral angles between in the range of 20 - 50° have been measured with light and low-resolution SEM microscopy (von Bargen and Waff, 1986; Beeman and Kohlstedt, 1993; Hirth and Kohlstedt, 1995). At low resolution the grain boundary wetness is underestimated. High resolution studies by scanning electron microscopy and TEM yield lower dihedral angle values of about 10° (e.g. Cmíral et al., 1998; Faul and Scott, 2006).

$In - situ$ observations on analogue materials (Walte et al., 2003, 2005, 2011) show that 'non-equilibrium' wetted grain boundaries are a consequence of steady-state grain growth (Walte et al., 2003, 2005, 2011). Layers on grain boundaries in olivine partial melts have been observed on 2-D images for example by (Faul et al., 1994; Faul and Fitz Gerald, 1999; Mu and Faul, 2016) and were confirmed by (Garapic et al., 2013) to represented wetted grain boundaries by serial sectioning. Implications of a more complex melt distribution characterised by contiguity, with implications for rheology (Mu and Faul, 2016), and seismic velocity and electrical conductivity, are summarised in review by Takei (2017). The observed complex melt distribution relative to the predictions of the simple isotropic model show that not all grain boundaries are equal, establishing the need to characterise the different grain boundaries and their distribution.

1.6 Grain growth

Grain growth is a result of Gibbs free energy (ΔG) minimisation of the total system where interfacial energies are included (e.g. Burke and Turnbull, 1952; Rollett and Rohrer, 2017). A brief review is given by Rollett et al. (2004) who

notes that 'the challenge is to establish a reliable structure - property relationship that includes all the relevant parameters such as temperature, composition and crystallographic type.' The main conclusion of this short review is, however, that 'simple models of grain boundary mobility do not provide an adequate description of the phenomenon.' This results in a continuos flow of studies on grain growth with the objective to describe both the coarsening rate and the grain size distribution with mathematical functions.

Full mathematically simulation of grain growth including the contribution of the interfacial energy reduction to the minimisation of the total Gibbs free energy of the system is available in multi phase field models, reviewed by Steinbach (2009). In these and other models the individual energy contributions can be incorporated - still anisotropy is only very seldom included (e.g. level-set method, Ghanbarzadeh et al., 2014). Many experimental studies have empirically determined the parameters for olivine grain growth under static conditions. Different factors where investigated: water (Karato, 1989; Ohuchi and Nakamura, 2007), oxygen fugacity (Nichols and Mackwell, 1991), melt (Cabane et al., 2005; Faul and Scott, 2006) and secondary phases, e.g. pores (Karato, 1989; Nichols and Mackwell, 1991), secondary phases such as orthopyroxenes (Hiraga et al., 2010; Tasaka et al., 2013) and clinopyroxenes (Ohuchi and Nakamura, 2007) and cation exchange (Ohuchi et al., 2010).

Abnormal grain growth can have different causes, but there must always be an energy or mobility advantage of the abnormally growing grain. Energy advantages can consist of a greater driving force for growth, for example through stored elastic or plastic strain energy, but also a lower surface energy causes faster growth. Mobility advantages mean that the abnormally growing grain has interfaces that are more mobile. This can be caused by an intrinsic structure of the grain boundary or by extrinsic solutes (incompatible elements) or particles on the grain boundary (e.g. chemical segregation, or particles, e.g. Figure 12). Abnormal growth occurs only when the growth advantage can persist while the grain grows into its neighbouring grains. Abnormal grain growth appears to be very rare, it is still observed in

natural olivine aggregates (e.g. Drury and Urai, 1990; Drury, 2005; Heilbronner and Tullis, 2006), in highly deformed aggregates during recrystallization in both *ceramics (Rollett, 2004)* and olivine Boneh et al. (2017). In the latter case it is taken responsible for orientation and magnitude of crystallographic preferred orientation and may influence the distribution and magnitudes of seismic wave velocities and anisotropies.

1.7 Rheology

1.7.1 Viscous regime

Convection in the Earth causes continuous, grain-scale deformation. Constitutive models for grain scale deformation can be derived for diffusion creep where diffusion occurs either through the grain interior (Nabarro-Herring creep) or along grain boundaries (Cobble creep), and dislocation creep which includes glide and climb Poirier (e.g. 1985). Experimentally the two mechanisms are distinguished by a) grain size dependence and linear stress dependence of diffusion creep, and b) grain size independence and a power-law stress dependence of dislocation creep. Dislocation accommodated grain boundary sliding is grain size-dependent but has a non-linear stress dependence (Hansen et al., 2011, 2012a).

Dislocation creep leads to grain size reduction through recrystallisation (accumulation of dislocations in sub grain boundaries, followed by rotation) where the recrystallised grain size is stress dependent (Karato et al., 1980; Van der Wal et al., 1993). Glide of dislocations includes a rotational component and consequent alignment of crystalline grains to produce crystallographic preferred orientation (CPO).

The rheology of partially molten rocks was investigated both experimentally Hirth and Kohlstedt (e.g. 1995); Mei and Kohlstedt (e.g. 2000); Faul and Jackson (e.g. 2007) and by modeling (e.g. Takei and Holtzman, 2009b). Currently constitutional laws of deformation including grain boundary processes are phenomenological with parameters that are not directly linked to atomic scale quantities. Obtaining

models that expand pure diffusion mechanisms to include grain boundary mechanisms (e.g. Ashby et al., 1970; Raj and Ashby, 1971; Ashby, 1972; Langdon, 2006) is a current goal of research (e.g. Cordier et al., 2014; Sun et al., 2016).

In diffusion creep, grain boundary sliding is a major strain producing mechanism necessary to explain equiaxed grain shapes even after large strains (superplasticity Miyazaki et al. (2013)). To explain powerlaw creep that is grain size dependent similarly grain boundary sliding is invoked (e.g. Hirth and Kohlstedt, 2003). Grain boundary mechanisms can relax the von Mises criterion (the need for five independent slip systems) in dislocation creep, as can the movement of grain boundaries, maybe facilitated by grain boundary disclinations (Cordier et al., 2014; Sun et al., 2016). In the case where grain boundary properties are strongly anisotropic, grain boundary mechanisms should allow energetically favourable interfaces to orient themselves to minimise the total viscosity of the aggregate (Maruyama and Hiraga, 2017b,a). Grain boundary deformation mechanisms are sensitive to the grain boundary structure (Cahn et al., 2006), and consequently also to the grain boundary viscosity (Maruyama and Hiraga, 2017b,a). Grain boundary structure in this context includes the roughness of the boundary, i.e. steps/facetts as mentioned in section 1.2.

1.7.2 Anelastic regime

While large strain deformation changes the grain scale microstructure, the microstrains due to the propagation of seismic waves interrogate the grain boundary properties without changing the microstructure. The model of accommodation of microstrains due to grain boundary sliding by Raj and Ashby (1971) includes two sequential processes. First, sliding of grain boundaries accommodated by elastic strain at grain corners or steps on grain boundaries. Due to the high elastic moduli the resulting strains are very small, particularly for small grain sizes.

Second, after the maximum sliding due to elastic accommodation has taken place, the resulting stress concentration at grain corners will drive diffusion, which

leads to a redistribution of stresses along grain boundaries towards the state of stress for macroscopic diffusion creep. This transient redistribution of stresses was termed diffusionally assisted grain boundary sliding by Morris and Jackson (2009) to distinguish it from macroscopic diffusionally accommodated grain boundary sliding.

Elastically accommodated grain boundary sliding and diffusionally assisted grain boundary sliding are both anelastic processes as the strain is recovered with a time delay on removal of the applied stress. Again grain boundary sliding is not directly observed in the experiments but inferred from the observed grain size dependence. An implicit assumption in the Raj-Ashby model is that grain boundaries are substantially weaker than grain interiors, consistent with the much higher grain boundary diffusivity. Diffusionally accommodated grain boundary sliding is inferred to account for the attenuation observed in torsional forced oscillations tests (Tan et al., 1997, 2001; Gribb and Cooper, 1998; Jackson et al., 2002), see the review by Faul and Jackson (2015). Grain boundary viscosities derived from small strain experiments in the anelastic regime are more than 5 orders of magnitude lower than steady state viscosities measured in diffusion creep (Faul et al., 2004).

2 Methods

Which sample type or preparation method is most appropriate for experimental studies has been debated for decades and regularly culminates in strong dissent between different research groups. The question is how a sample should be best prepared to best simulate natural samples, while having small grain sizes, mosaic (foam) texture, indicative of steady state grain growth, often referred to as equilibrium texture (technically wrong, but descriptive for the sluggish grain coarsening) and controlled impurities. Depending on the question to be addressed the different samples preparation methods all have their advantages and disadvantages. Natural samples are too coarse-grained, the presumably representative composition led to

samples that are reconstituted from ground and hand sorted grains to have both, small grain sizes and natural composition. The compositional range is variable depending on source materials and quality of sorting. The grinding may cause the introduction of dislocations. It is often critically commented that reconstituted samples may not reach micro-structural "equilibrium" before the actual experiments are performed (e.g. Mcdonnell and Spiers, 2002; Sano et al., 2006; Koizumi et al., 2010). Solgel samples (e.g. Edgar, 1973; Jackson et al., 2002) and vacuum sintered samples (e.g. Koizumi et al., 2010) can result in very fine grained and micro-structurally "equilibrated" samples. However, the applicability of experimental observations on iron-free systems to natural systems is highly debated, since diffusion mechanisms differ strongly in the iron-free and iron-bearing systems (Chakraborty et al., 1994; Chakraborty, 1997; Petry et al., 2004). While vacuum sintered samples are still iron-free, solgel samples with and without iron and representative trace element impurities (e.g. Faul et al., 2016) have been prepared. Note that Chakraborty (1997) concluded that the iron-related point-defect dependent diffusion mechanism, at constant P, T, f_{O_2} and a_{Si} is dominating over all trace-element related point defect diffusion mechanisms. Therefore, the sole presence of representative amounts of iron and defined P, T, f_{O_2} and a_{Si} might suffice to simulate natural diffusion related processes. Nevertheless, studying the effect of iron and individual trace elements simplifying the final interpretation is necessary to prove this assumption. Finally, for the study of grain boundaries bicrystals can be synthesised, where the interface has the orientation of choice (e.g. Heinemann et al., 2005; Hartmann et al., 2010; Marquardt et al., 2011d,c). In the following we examined different samples of different preparation origin to compare the grain boundaries at the nm-scale using transmission electron microscopy.

Reconstituted rocks (RR): Samples for deformation or attenuation experiments are produced by selecting olivine crystals of several mm in size that are as inclusion-free as possible. These crystals are then crushed and sorted by size before being cold pressed to 200 MPa and hot-pressed in a cylindrical shape for deformation.

Typical sample sizes of 10 - 11.5 mm in diameter and 20 - 30 mm in length require substantial amounts of starting material. Even careful hand-picking of the original grains as well as of the crushed fragments under a binocular microscope typically does not reliably remove all incorporated other phases. The resulting sample aggregates contain variable amounts of melt at high temperatures ($\sim$1250$^{\circ}C$) and low pressure ranging from 0.01 $wt.\%$ or less (Tan et al., 2001; Faul et al., 2004) to $\sim$ 1 $wt.\%$ (Karato et al., 1986; Hirth and Kohlstedt, 1995; Mei and Kohlstedt, 2000).

Solution gelation derived samples (SG): Fully synthetic samples are produced from reagent grade nitrites and ethanol solutions, which are reacted and fired to produce fine-grained starting materials (Jackson et al. (2002, 2004)). These materials are consistently melt-free at the TEM scale (Faul et al. (2004)). The deformation experiments discussed below were conducted in a Paterson gas-medium apparatus at 300 MPa confining pressure. The experimental procedures are detailed in Faul and Jackson (2007). Sample 1623 contains 396 ppm Ti/Si, 780 ppm H/Si, and has an average grain size of 21 μm.

Vacuum sintered samples (VS): Nano-sized powders of colloidal SiO_2 and highly dispersed $Mg(OH)_2$ with particle size of less than 50 nm were used as chemical sources for MgO and SiO_2. They were cold-pressed and vacuum sintered to obtain highly dense and fine-grained polycrystalline samples (Koizumi et al., 2010), the transmission electron microscope study was performed on one of the samples from a different study (Fei et al., 2016) and more details are available in this study.

Wafer bonded bicrystals: One sample was produced using the wafer bonding method (Heinemann et al., 2001, 2003, 2005; Hartmann et al., 2010; Marquardt et al., 2011c,d), where two epi-polishe forsterite surfaces saturated with pure adsorbed water are brought into contact without force. Additional annealing establishes atomic bonds across the interface. The forsterite was grown at the institute for

crystal synthesis (IKZ-Institut für Krizstallzüchtung Berlin) using the Czochralski method (Czochralski, 1918). Here we produced a 60° [100]/(011) grain boundary.

3 Analysis

Generally all samples were investigated with a combination of methods ranging from light microscopy, microprobe wavelength dispersive spectroscopy (WDS) and energy dispersive spectroscopy (EDS) in both scanning electron microscopy (SEM) and transmission electron microscopy (TEM).

Prior to *EBSD measurements*, the studied samples were chemo-mechanically polished for 2-8 h using an alkaline solution of colloidal silica on a soft substrate. The crystallographic orientation measurements were carried out on 3-6 nm carbon-coated samples using automated indexing routines commercially available. Most of the EBSD analyses were conducted using a FEI Scios FEG dual beam machine at Bayerisches Geoinstitute. The system is equipped with an EDAX-TSL Digiview IV EBSD detector and the OIM software incorporated in the TEAM 8 user interface. Simultaneous acquisition of energy dispersive X-ray spectra for each orientation measurement point allowed to exclude pyroxene from the indexing routine, because we only analysed the olivine GBCD form these data. We simply excluded all data points where the Si to Mg ratio was closer to 1:1 than 1:2. Our mappings where conducted at accelerating voltage of 20 kV, beam current of 3.2 nA and working distance of 10-14 mm. We used step sizes of at least 1/10th of the grain size, thus varying from 0.2 μm to 1 μm using a hexagonal mapping grid. Olivine was indexed in space group Pbnm using the lattice constants a = 4.762 $\mathring{A}$, b = 10.225 $\mathring{A}$, and c = 5.994 $\mathring{A}$.

Data treatment: From EBSD maps we reconstructed the grain boundaries using the OIM analyses 8. Grains were defined with a minimum disorientation of 3°, and this fixes the lower limit for the smallest grain boundary disorientation. We did two runs exporting the grain boundary segments, once including the low angle grain boundaries (3-20° disorientation), once we only considered grain

sample name	**type**[a]	**trace elements**[b]	**grain size,** μm	**melt content,** $wt.\%$	**T** $(^\circ C)$**, duration**[c] (h)	**capsule material**	**figure**	**ref**
6261	Fo_{90} RR	natural	23.4	<0.01	1300, 36	Fe	14	Jackson et al. (2002)
6381	Fo_{90} SG	undoped	2.9	melt-free	1200, 46	$Ni_{70}Fe_{30}$	8, 14	Jackson et al. (2002)
6366	Fo_{90} RR	natural	52.3	0.4	1240, 110	$Ni_{70}Fe_{30}$	14	Faul et al. (2004)
6384	Fo_{90} SG	melt-added	27.5	3.7	1300, 42	$Ni_{70}Fe_{30}$	8, 14	Faul et al. (2004)
6525	Fo_{90} SG	undoped	4.0	melt-free	1300, 24	$Ni_{70}Fe_{30}$	10a	Faul and Jackson (2007)
6614	Fo_{90} SG	0.1 wt. % CaO	3.9	melt-free	1250, 30	$Ni_{70}Fe_{30}$	16	this study
6615	Fo_{90} SG	0.1 wt. % CaO	5.9	melt-free	1300, 30	$Ni_{70}Fe_{30}$	16	this study
6617	Fo_{90} SG	0.1 wt. % CaO	3.2	melt-free	1200, 30	$Ni_{70}Fe_{30}$	16	this study
6767	Fo_{90} SG	261 wt. ppm Ti	15.7	melt-free	1200, 40	Pt	12, 13	Faul et al. (2016)
6713	Fo_{90} SG	216 wt. ppm Ti	6.7	melt-free	1300, 30	$Ni_{70}Fe_{30}$		Faul et al. (2016)
6714	Fo_{90} SG	216 wt. ppm Ti	6.5	melt-free	1200, 30	$Ni_{70}Fe_{30}$		Faul et al. (2016)
1623	Fo_{90} SG	396 wt. ppm Ti	21	melt-free	1300, 31	Pt		Faul et al. (2016) Fei et al. (2016) Koizumi et al. (2010)
P4	Fo_{100} VS	undoped	6.4	melt-free				Tasaka et al. (2013)
fo_bi_011	Fo_{100}	undoped	mm	melt-free	1640, 48	Pt	15	

a RR reconstituted hot pressed rock from San Carlos olivine powder,
SG solgel origin, VS vacuum sintered. Mg-numbers are rounded values.
In detail SG samples tend to be somewhat lower (to 89.5), RR somewhat higher (to 90.5)
b Natural: (San Carlos olivine) Al, Ca, Ti, Na, Cr, Mn, Ni, Co, Zn, P, Sc
(e.g. Garrido et al., 2000; Davies et al., 2006; Lee et al., 2007; Drouin et al., 2009; De Hoog et al., 2010; Foley et al., 2011, 2013).
Melt added: derived from composition of added basaltic melt (Al, Ca, Ti, Na, K).
c Duration of exposure to highest temperature

Table 1 Compilation of parameters for sample synthesis and references to other studies where data from the same samples have been published.

boundaries with disorientations larger than 20°. This follows the observation that individual dislocations can be distinguished for disorientation angles as large a 20° (Heinemann et al., 2005), which defines the transition from low- to high-angle grain boundaries.

The quality of the indexing of the Kikuchi-patterns is expressed as confidence index (CI) ranging from 0 to 1, where values above 0.2 are sufficient for correct indexing. Our CI values were generally higher than 0.2. Generally we obtained maps with very high indexing fractions (∼95% of the pixels), and little misindexing. We performed a clean-up procedure to remove unindexed and misindexed pixels: First we applied a correction for pseudo-symmetry, e.g. 60° about [100]. Furthermore, we dilated grains to absorb points not belonging to any grain (defined as a minimum of 2 neighbouring points with the same orientation within 3°) which frequently occur along grain boundaries where two Kikuchi pattern overlap. For pixels at boundaries, the isolated point becomes part of the grain that surrounds the majority of the point; if two grains surround the individual points equally, the point becomes part of the grain with the highest average CI. The absorbed point takes orientation and CI of the neighbouring grain with highest CI. Dilatation was set to result in a minimum of 3 rows of a minimum of 3 pixels each, which did not affect the average grain size determined before and after this procedure. Note, that the grains considered for further analyses were chosen to have a minimum size of 25 pixels over at least three rows. The grain boundary traces are reconstructed into segments. Triple junctions are identified and a straight line is drawn between them. The segments are dissected into shorter segments. The tolerance between the reconstructed line and the actual grain boundary is less than twice the step size used for mapping, a schematic explanation is given by others (Edax OIM analyses 8 manual). Subsequently the exported grain boundary line segments were evaluated using the scripts developed at the Carnegie Mellon University, Pittsburgh (Rohrer et al., 2004).

Electron microprobe analyses (EMPA) Microprobe analyses were performed at the MIT Electron Microprobe Facility on the JEOL-JXA-8200 with 15 kV acceleration potential and a beam current of 10 nA and a beam diameter of $\sim$ 1 μm. Counting times were 20-40 s per element, resulting in counting precisions of 0.5-1.0 % 1-σ standard deviations. The raw data were corrected for matrix effects with the CITZAF program (Armstrong, 1995).

Transmisssion electron microscopy (TEM) TEM investigations were performed with a FEI Titan^{TM} G^2 80-200 microscope at Bayerisches Geoinstitut Bayreuth, using conventional TEM, high resolution (HR)-TEM as well as scanning (S)-TEM modes. The microscope was operated at an acceleration voltage of 200 kV with an electron beam generated by an extreme brightness field emission gun (X-FEG) Schottky electron source. The point resolution is 0.24 nm, and 0.16 nm STEM resolution. The TEM is equipped with a post-column Gatan imaging filter (GIF Quantum^{R}SE). Analytical TEM was performed in scanning transmission mode, STEM. The probe size after careful optimisation is 160 pm, and the final image resolution in STEM results from pixel size and probe size. The signal is acquired using a high angle annular dark field detector (HAADF), with the camera length optimised to yield Z-contrast. Energy dispersive X-ray spectra were acquired using a windowless SuperX-EDS detector with 4 Si-drift detectors (SDDs) inclined towards the sample in a superimposed circle, resulting in 0.7 $srad$ solid angle for collection. This configuration allows acquisition of high numbers of X-rays and facilitates to obtain reliable peak to background ratios, thus overcoming previous difficulties (e.g. Kohlstedt, 1990). The EDS analyses are point analyses, smart line profiles (Sader et al., 2010; Marquardt et al., 2011d) a method largely comparable to the elliptical beam analyses of previous studies (e.g. Drury and Fitz Gerald, 1996). The area measured is usually wider than the grain boundary region, so that the resulting analysis is a mixture of grain boundary and grain interior volumes. This means that the absolute compositions of the grain boundaries can only be obtained through lengthly extrapolations by

measurements with different beam sizes and extrapolating down to the width of the grain boundary. As the current paper is a compilation of previous results and aims at a qualitative summary extended with new data we refrain from quantitative analyses. The map in Figure 14 the area of interest was scanned for 2 hours continuously; the spectra at each pixel are summed. Each pixel has a size of 4 nm.

High resolution transmission electron microscopy (HRTEM) In order to image the structural width of a grain boundary using HRTEM, the grain boundary has to be parallel to the electron beam (edge-on condition). This condition can be tested using the appearance of fresnel fringes when bringing the sample in an out of the minimum contrast condition. Note that delocalisation is more pronounced for large reciprocal space vectors (i.e. small lattice spacing). Dark or bright fresnel fringes appear on both sides of the grain boundary at the same distance when changing the defocus; however if the grain boundary is not edge-on the fresnel fringes will have different grayvalues on either side of the interface and may also have different widths and distances from the interface (Figure 4). It was previously pointed out (Hiraga et al., 2002) that a grooved surface, even in the absence of a glass film, can produce Fresnel fringes with contrast stronger than that produced by a glass film at a grain boundary (Rasmussen et al., 1989). Thus the Fresnel fringe method is not the best to determine whether or not an amorphous film is present, but assuming that such grooves are relatively symmetric they are still suitable to test the inclination of the interface. The defocus is chosen to lie between Scherzer (for maximum resolution) and 0 to minimise delocalisation (Williams and Carter, 2009; B. Fultz, 2001). This is the optimal focus for direct image interpretation for uncorrected transmission electron microcopy to image interfaces.

Lattice planes can only be resolved by high resolution transmission electron microscopy (HREM) if they are close to fulfil the Bragg criterion and thus waves interact constructively. The contrast can be interpreted directly up to the point resolution of the microscope. Interpretation of higher frequencies require image

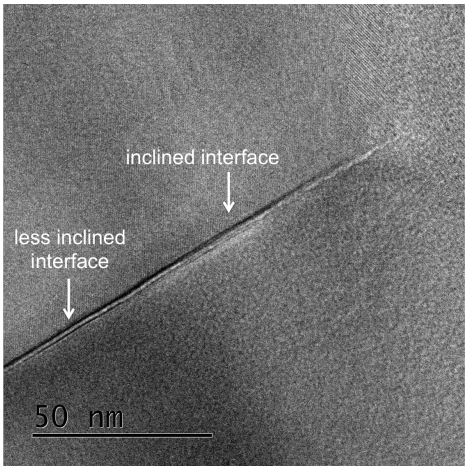

Fig. 4 High resolution TEM images of grain boundary that changes inclination with respect to the incident electron beam. The fresnel fringes vary in intensity and grayscale where the grain boundary plane is strongly inclined with respect to the incidence beam direction. The Fresnel fringes change width at a less inclined areas of the interface.

simulation and exit wave reconstruction (e.g. Marquardt et al., 2011d; B. Fultz, 2001; Williams and Carter, 2009).

To use the resolution of the microscope to its point resolution while minimising delocalisation we used a virtual aperture of $\sim 3.33\ nm^{-1}$ by post processing to remove frequencies that result in delocalisation greater than $0.9\ nm$. In order to observe lattice planes on both sides of a grain boundary and simultaneously have the grain boundary plane parallel to the beam, the grain boundary must be oriented in a relatively low index zone common to both crystals; this is a relatively rare condition that is not met for the vast majority of grain boundaries. The orientation requirement for the grain boundary plane is quite stringent: Vaughan et al. (1982) pointed out that in order to resolve a $1\ nm$ wide layer, the grain boundary has to be oriented with an accuracy of better than 2° for a $30\ nm$ thick TEM foil. Therefore several authors previously gave direct recipes on how to acquire best HRTEM images of interfaces Clarke (1979a); Vaughan et al. (1982); Hiraga et al. (2002). In short they contain the following steps:

1. Find a thin grain boundary in good orientation to fulfil the above mentioned criteria.
2. Correct astigmatism of the condenser and objective lenses close to the region of interest.
3. The chosen diffracted beams of both crystals must be accurately centred in the objective aperture and remain on the optical axis of the microscope, you may follow the illustrated examples given in Vaughan et al. (1982).

4. Allow the frequencies necessary for imaging to pass through the aperture, preferably up to the inverse of point resolution for uncorrected microscopes. The optimum can be calculated using equation 28.72 in Williams and Carter (2009).
5. Acquire a through-focus series to subsequently choose the image with the optimum defocus conditions.

Note, if a sample allows for acquisition of HRTEM images at different defocus values, and thus reconstruction of the exit-wave is possible, phase images with minimised delocalisation can be calculated. Alternatively, spherical aberration (Cs)-corrected microscopy allows acquisition of images that are nearly free of delocalisation. Other STEM based methods to retrieve the thickness and orientation of interfacial layers have been proposed (Koch et al., 2006; Kiss et al., 2016). If beam damage is not an issue, these have significant advantages, for example that they result in little delocalisation.

Deformation experiments were conducted in a Paterson-type gas-medium apparatus (Paterson, 1990). The samples were tri-axially compressed at a confining pressure of 300 MPa. The temperature was controlled using a Eurotherm controller and a type R Pt-Rh thermocouple. The load cell was calibrated and for jacket corrections samples of mild steel were deformed that have similar composition as the here used mild steel jackets. More details are described in Faul and Jackson (2007).

4 Results

4.1 GBCD of sol-gel derived Fo_{90}

The full five parameter grain boundary character for a the sol-gel derived Fo_{90} sample, with less than 2 vol.% of pyroxene was determined using EBSD mapping and stereological analyses of over 200.000 grain boundary segments. The most important observations of the sample are summarised in Figure 5a-d. In Figure 5a the disorientation distribution as a function of the total measured grain boundary length is displayed. The measured disorientations between adjacent crystals is plotted in red and compared to the calculated Mackenzie distribution for randomly

oriented orthorhombic crystals in blue (Mackenzie, 1958). Our sample shows perfect agreement with the calculated random distribution and orientation distribution functions yield no LPO. In Figure 5b the axes angle distribution, e.g. three independent parameters for each grain boundary is displayed. All axes of rotation for the disorientation angles 10°, 60°, 90° and 110° are displayed. No marked preference for any specific axis of disorientations is observed for 10°, 90° and 110° disorientations, only 60° disorientations show a preference of being rotated around the [100] axis, similar to previous observations (Faul and Fitz Gerald, 1999; Marquardt et al., 2015). This is of cause after correcting for all pseudo-symmetric misindexing.

Grain boundary planes dominating the interfacial network are displayed in Figure 5c. Grain boundaries close to perpendicular to the c-axis dominate the distribution, with a maximum near (012)-planes. Generally the grain boundary planes show a preference for planes along the edge [001] to [010] of the standard triangle for orthorhombic crystal systems. Therefore (0kl)-type planes make up the largest portion of the surface area of olivine cystalls in this polycrystal. The planes most frequently brought into contact by a 60° rotation about the [100]-direction are displayed in Figure 5d. In agreement with the high occurrence of (0kl)-type boundaries this specific axis angle pair favourably involves planes of (0kl)-type.

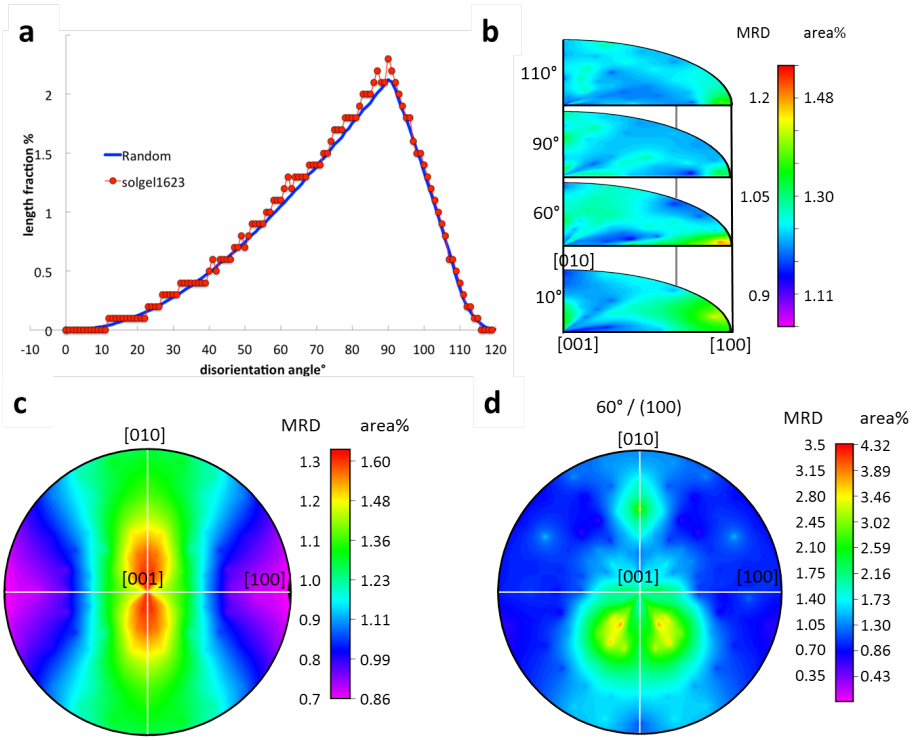

Fig. 5 Different representations of information about grain boundaries in solgel derived Fo_{90}, all from the same data. a) Single parameter disorientation distribution in red, each grain boundary is reduced to its minimum disorientation angle, disregarding its disorientation axis. The random distribution is shown in blue for comparison. b) Three independent parameters for each boundary are given in the axis angle representation of the disorientation. Two parameters for the axis direction and one for the rotation angle. Each point in 3D space represents one individual grain boundary, that is distinct from the next. In each of the layers of the axis angle space all possible axis are presented. Each layer corresponds to a different rotation angle which varies at non-constant intervals along the vertical direction. Note, that there are only very slight preferences for specific rotation about specific angles. The 60° rotations mostly occur around the [100] and 10-20° rotations have a preference for [100] and/or [210]. It should be noted that only a very small fraction of all grain boundaries of this sample are low angle grain boundaries, consequently the statistical relevance of the information obtained for this range is limited. c) Grain boundary plane distribution irrespective of disorientation. It yields an approximate average crystal habit. d) For any particular axis angle combinations a specific grain boundary plane distribution exists, here it is shown for 60° about the [100] direction. We chose to display only planes in 60° about the [100], because only planes with this specifc disorientation angle shows a significant preference for a specific axis of rotation. The color code in the stereographic plots gives values in multiples of random distribution (MRD) and the respective area %.

4.2 Direct micrographs of grain boundaries

In order to obtain the most representative information about variable grain boundary structures grain boundaries were chosen arbitrarily (with the only criterion of being at the thinnest areas of the TEM-lamellae). The grain boundary was oriented parallel to the beam and subsequently rotated about the axis perpendicular to the grain boundary until lattice fringes could be observed. This procedure often results in images where lattice fringes, with frequencies (d-spacings) that do not suffer from delocalisation are visible only in one of the grains, as most of the time the second grain is in an orientation where non of the planes with large d-spacings are parallel to the beam (Figure 6d, 7 and Figure 8a,b). The width of the grain boundary region in the resulting images ranges up to 1 nm. In some micrographs the grain boundary region does not display any lattice fringes and appears amorphous. These grain boundary images are subsequently called 'amorphous' type. The imaged width of 'amorphous' appearing grain boundaries is independent of sample type (i.e. synthetic Fo_{100}, Figure 6d, synthetic Fo_{90}, Figure 8a, or San Carlos derived reconstituted rocks, Figure 8c). The presence of melt in a sample similarly does not influence the width of the grain boundary region of non-wetted grain boundaries in the micrographs (Figure 8b). Similar images were also published Faul et al. (2004) from solgel samples with added melt and Mei and Kohlstedt (2000) from experimental samples with olivine of natural origin.

Figure 7 shows a straight grain boundary with varying grain boundary outline from top, with a smooth grain boundary to bottom with a stepped/facetted appearance. Note that the right grain has relatively large d-spacings, which generates the impression of steps at the interface. This impression is however misleading, because other crystallographic planes, less easily identified by eye because of there smaller d-spacing are continuous and more parallel to the grain boundary. In the upper part of the micrograph, where these d-spacings are better visible the grain boundary appears very smooth.

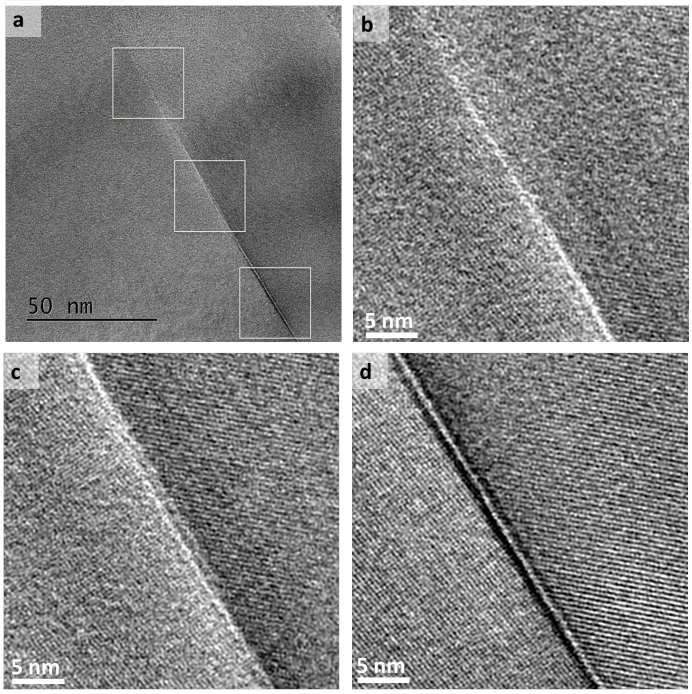

Fig. 6 HRTEM micrograph of vacuum sintered Fo_{100} from the Hiraga Lab. The grain boundary is parallel to the incident beam, lattice fringes are obtained for both crystals. a) The contrast changes along the grain boundary with increasing sample thickness towards the bottom of the image. Frequencies corresponding to d-spacings of less then 0.24 *nm* are removed using a Fourier filter, because they suffer from delocalization. This procedure is analogous to placing an objective aperture in the back focal plane of the objective lens. In b and c the lattice planes of the adjacent crystal lattices are in 'contact'. In c a facet at the centre of the micrograph results in a double line along the interface. The region between the fresnel fringes in d might appear amorphous if a too large aperture were used. Figure 1 of Fei et al. (2016) stem from the same study. The original images are displayed in Figure 18 of the appendix.

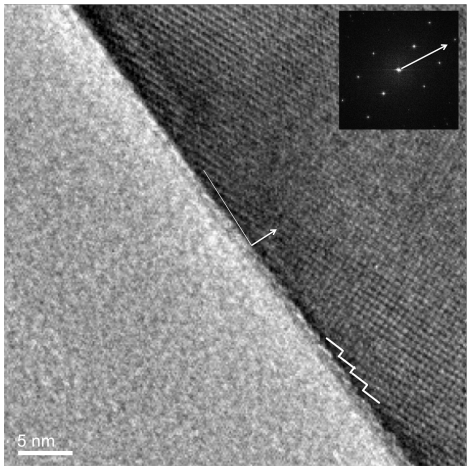

Fig. 7 HRTEM micrograph of a vacuum sintered sample. The grain boundary is parallel to the incident beam, lattice fringes are obtained for both crystals, even thought those on the left crystal have such small d-spacings that they are nearly not resolved anymore. The right grain has relatively large d-spacings. In the upper part of the micrograph the grain boundary thus appears very smooth.

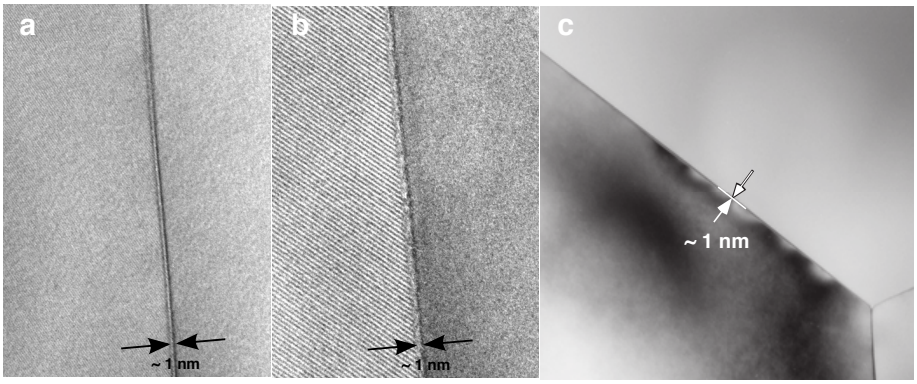

Fig. 8 High resolution TEM images of grain boundaries in polycrystalline olivine aggregates. The width of the grain boundaries (oriented parallel to the electron beam) is about 1 *nm* for all samples (note that the scale of the each image is different). **(a)** Melt-free solgel sample 6381 with lattice fringes resolved in the left grain (Jackson et al. (2002)). **(b)** Melt-added solgel sample 6384 with lattice fringes resolved in the left grain (Faul et al. (2004)). (**c**) San Carlos olivine sample 6261 with a melt content $< 0.01\%$ (Tan et al. (2001); Jackson et al. (2002)).

Figure 8 is a compilation of previous micrographs published as indicated in the figure caption. The two melt-free grain boundaries in Figure 8a and 8b appear similar even though the former is from a melt-free solgel sample, while the latter is from a melt added solgel sample. Therefore, the images by themselves provide no indication of the provenance or state (melt vs. no melt) of the sample.

In contrast Figure 6b,c, 9 and Figure 10a show directly abutting lattice planes for both olivine grain boundaries and olivine enstatite phase boundaries, where similar micrographs where also published in Vaughan et al. (1982); Hiraga et al. (2002), subsequently called 'crystalline' type. Note that both types of grain boundary micrographs can be obtained from the same grain boundary as shown in Figure 6. In 6b and c the grain boundary appears 'crystalline', while in 6d it appears 'amorphous'. The different appearance is a consequence of contrast that depends on defocus setting and sample thickness. Note that the 'crystalline' interpretation is more appropriate, as 'amorphous' is observed in sample regions more easily biased by imaging artefacts (e.g. thicker sample). Note that the grain boundary displayed in Figure 6 is mostly straight, expect for 6c where a facet is observed, that causes the boundary to appear as a double fringe in the centre of the micrograph.

The grain boundary planes in the synthetic forsterite bicrystal of Figure 9 are the (011) planes with respect to both adjacent crystals. The planes is brought into contact by a 60.8° rotation about the common [100] axis. The here imaged grain boundary is facetted on the nm-scale. Two inclined areas are visible. The structural width of the grain boundary at places oriented parallel to the electron beam is less than 1 nm. The adjacent crystal planes are in direct contact.

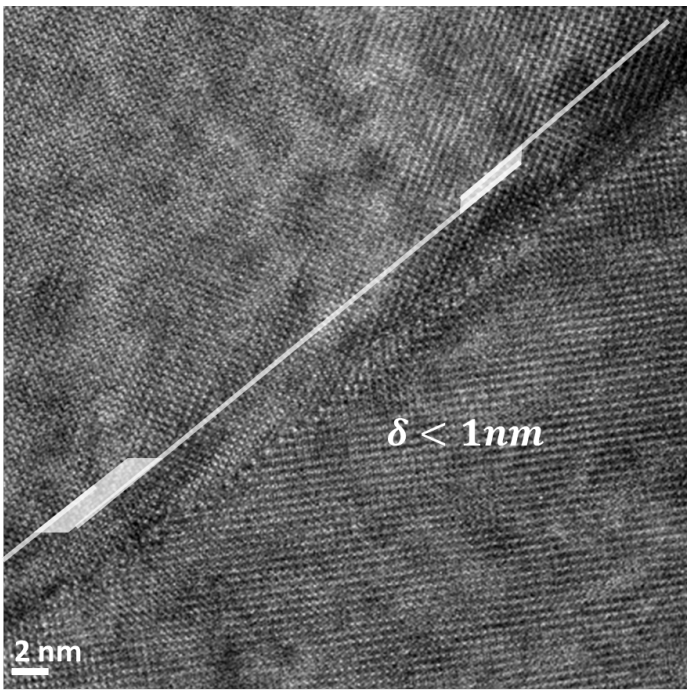

Fig. 9 HRTEM micrograph the synthetic forsterite bicrystal, the grain boundary plane is the (011) with respect to both adjacent crystals. The grain boundary was traced in transparent white and the inclined facets are indicated by shaded regions - the traces where then shifted with respect to the grain boundary to allow the reader to have a better view of the structure. The structural width of the grain boundary is less than 1 nm and thus of 'crystaline' type. The adjacent crystal planes are in direct contact.

In Figure 11 a phase boundary between forsterite and enstatite in solgel sample 6793 where elevated Ti-levels were measured is displayed. The lattice planes of both phases are in direct contact. Which lattice planes appear clearly in the crystals is again caused by sample thickness and defocus setting. Note the small dark region in Figure 11c. In Figure 12 a similar phase boundary of the same sample is depicted. The enstatite can be easily distinguished from olivine due to its twin lamella. These are common observations in enstatite, a result passing the phase transition from orthoenstatite to clinoenstatite during quenching. These lamellae are also

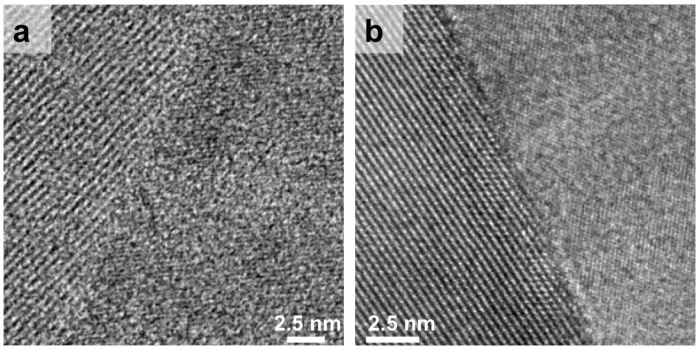

Fig. 10 HRTEM micrograph of a) an olivine grain boundary of solgel sample 6525. The width of the grain boundary is less 1 *nm* and appears as part of the 'crystalline' type. b) Forsterite enstatite phase boundary. Lattice fringes are in direct contact.

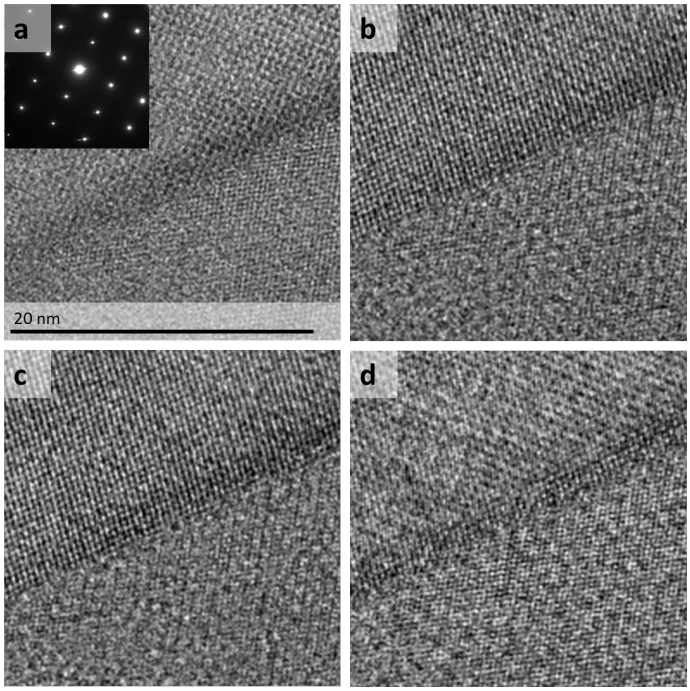

Fig. 11 HRTEM micrograph at slightly different positions along the wedge shaped solgel sample 6793, see Table 1. The changing sample thicknesses influences which lattice planes are more apparent in the image. The inset in a) is a selected area diffraction (SAD) pattern of the olivine. In centre of the micrograph in c) a small dark area is visible. Generally the lattice fringes of enstatite and olivine are in direct contact. No amorphous layer is observed.

present in the previous HRTEM images, but are more difficult to see: look at a printed micrograph at different inclinations. The observable features are given in Figure 12d. The interface - phase at the olivine - enstatite - phase boundary forms lower dihedral angles with the olivine, while having a droplet shape towards the enstatite. During the investigations in the TEM the operator had the impression that the particles are crystalline, this is supported by the diffraction contrast reversal from Figure 11a to Figure 11b, but absolute prove of crystallinity is not

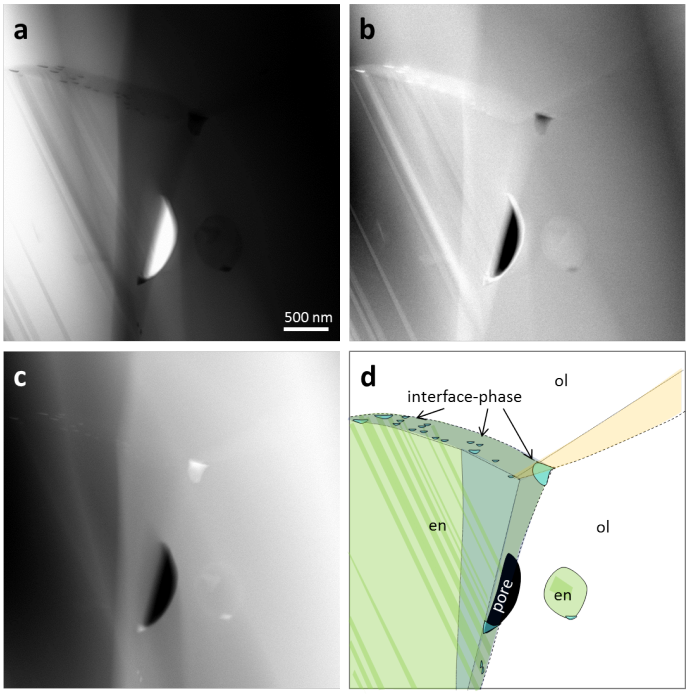

Fig. 12 Scanning transmission electron micrographs of an olivine grain boundary and two olivine- enstatite phase boundaries. Solgel sample 6793, see Table 1. a) BF b) DF c) HAADF. d) schematic of the phase assemblage; ol-ol-grain boundary, orange; ol-en-interphase boundary, blue-gray; enstatite in green with twin lamellae; olivine, colourless.

provided. At the triple junction where two olivine-enstatite phase boundaries and one olivine - olivine grain boundary meet, the dihedral angles are sensitive to the type of interface. The dihedral angle of the interface - phase with the enstatite is large whereas it is low for the olivine grain boundary (yellow). The latter angle is smaller than 60°. The shape of the pore may not be interpreted directly, as the wedge shaped TEM lamellae has been preferentially thinned in the vicinity of the pore, which makes interpretation more difficult. Figure 13 shows similar particles at olivine grain boundaries. They are however surrounded by amorphous material 13c,d and display equal dihedral angles towards both crystal surfaces.

4.3 Grain boundary composition

Grain boundaries and interiors of solgel as well as San Carlos olivine were analysed by TEM and microprobe, respectively. Grain interiors of undoped solgel without

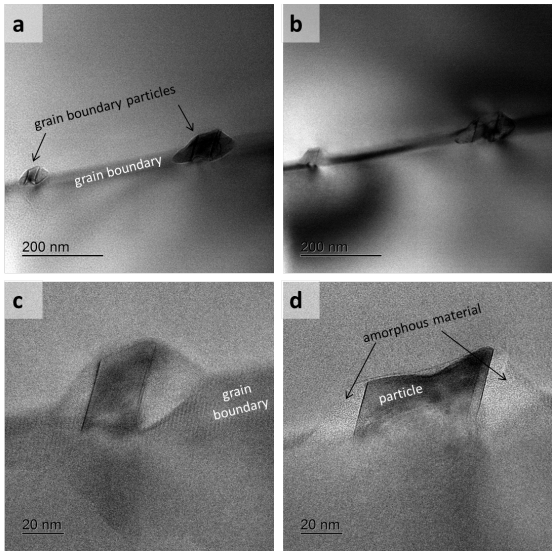

Fig. 13 Ti-Fe-rich particles at an olivine grain boundary in solgel sample 6793, see Table 1. The micrographs are representative for particles found on most olivine grain boundaries in this sample. They are facetted and embedded in an amorphous material. Bright field images a,b) of two grain boundary particles, the sample has been tilted in between the image acquisition, thus the diffraction contours have moved, highlighting the crystalline nature of the particles in contrast to the amorphous surrounding. a) was acquired with a large defocus, thus Fresnel fringes are visible surrounding the particle and the amorphous phase. High magnification bright field images c,d) of the two particles visible in a,b).

added melt contain no detectable trace elements. Correspondingly, TEM grain boundary analyses also show no detectable trace elements (Figure 16, the orange box).

Elements that are relatively incompatible in olivine, for example Ti, segregates to the grain boundaries. The measurements presented in Figure 14 originate from a pure Fo_{90} solgel sample that was doped with $0.04 wt.\%$ Ti. The mapping shows a small angle grain boundary in contact with a high angle grain boundary. The crystal interior and the low angle grain boundary show no detectable Ti while the high angle grain boundary region is enriched in Ti. This is even clearer when integrating the signal over larger regions, Figure 14b.

When melt with the same basaltic composition was added prior to hotpressing, both San Carlos olivine and solgel olivine equilibrate with the melt, containing for example 0.2 $wt.\%$ CaO in grain interiors. Correspondingly, their grain boundaries are enriched in Ca, Al, and Ti (Figure 15). San Carlos olivine to which no melt has been added contains less Ca, Al and Ti at grain boundaries than melt added samples (Figure 15). This correlates with their lower total trace element contents

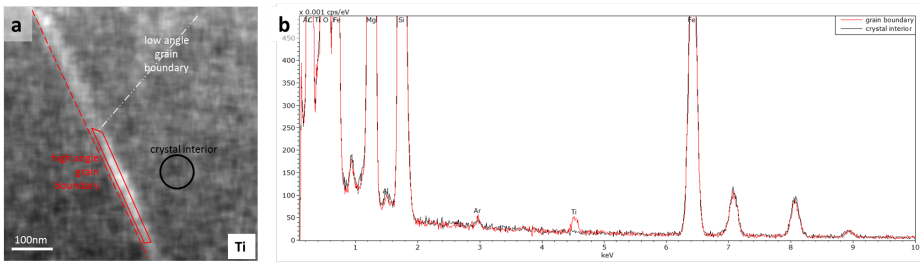

Fig. 14 a) Titanium distribution map obtained by EDS in scanning TEM mode. The whiter the map, the higher is the concentration of Ti. In b) the integrated spectra from the regions indicated in a), which cover the same area, are displayed. The spectra show absolute counts versus energy in keV. The high angle grain boundary shows a considerable concentration of Ti, red spectra. While the crystal interior indicates only statistical back ground counts. These are raw data.

966 in the grain interiors. Melt added San Carlos and solgel olivine contain similar
967 amounts of trace elements in their grain boundaries.

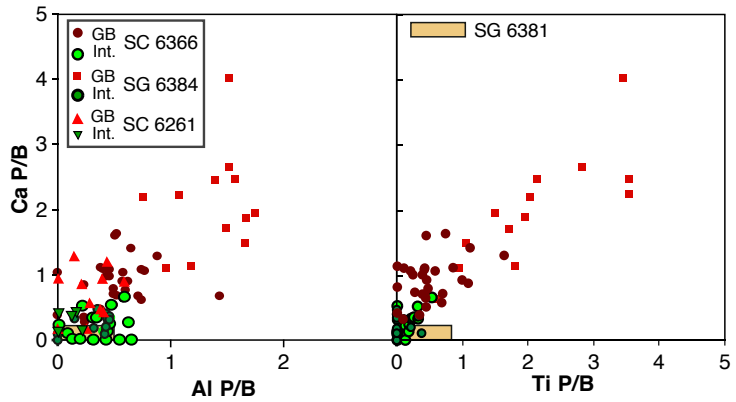

Fig. 15 TEM-EDS Analyses of grain interiors and grain boundaries. The peak to background (P/B) ratios of the spectra show that Ca, Ti and Al are enriched in grain boundaries (red symbols) relative to grain interiors (green symbols). The two San Carlos samples have similar Ca and Al contents in grain boundaries, lower than melt-added solgel olivine. The grain boundary concentrations correspond to the concentration of trace elements in grain interiors (Table 1). The Ti content of 6261 was not determined. Analyses of grain boundaries of undoped, melt-free sample 6381 are indicated by the box.

968 Figure 16 shows grain boundary analyses of a sample made from San Carlos
969 olivine that was first hot pressed with basaltic melt added, deformed, and finally
970 again annealed. After each step a section of the sample was taken for analysis.
971 During the initial hot pressing grains grew to about 100 μm. During the subsequent

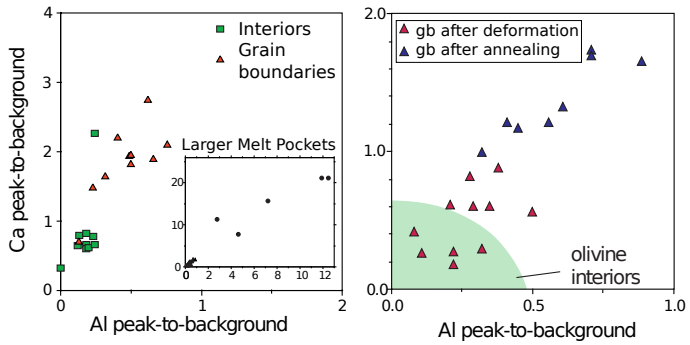

Fig. 16 Analyses of grain interiors and grain boundaries by TEM-EDS of a sample hotpressed for 240 hours at 1200°C **(a)** and **(b)** after deformation at 1250°C to 35% strain in triaxial compression (red triangles) and annealing for ∼ 500 h at 1300°C in a piston cylinder apparatus (blue triangles). The inset in **(a)** shows the concentrations of Ca and Al in large melt pockets. Newly formed grain boundaries have trace element contents comparable to grain interiors, but after equilibration at high temperature their trace element contents return to the higher level of undeformed samples.

deformation at differential stresses up to 250 MPa the sample recrystallized extensively to a mean grain size of 20 μm. During annealing the grain size increased again to 50 μm. Figure 16a shows that after hot pressing the grain boundaries are similarly enriched in Ca and Al as melt-added solgel sample 6384 (Figure 15). For comparison, the inset shows the much higher concentration of these elements in bulk melt from micron-sized melt pockets.

Grain boundary composition and deformation: Figure 16b shows grain boundary compositions after deformation and after the subsequent annealling. The grain boundaries formed during deformation due to sub-grain rotation and migration contain initially lower levels of impurities, more similar to grain interiors. During annealing the concentration of trace elements in grain boundaries increases again to levels somewhat below those found after hot pressing. Similar trend is observed in the deformed solgel sample 6767 where Ti segregated to high angle grain boundaries but low angle grain boundaries have similar Ti concentration as the crystal interior (non detectable), Figure 14.

Deformation experiments on Ca and Ti - doped solgel Fo_{90} samples were performed at temperatures between 1200 and 1300°C, in the diffusion creep regime.

989 The amount of Ca dopant is similar to that found in olivine from relatively fertile
990 peridotite xenoliths (Witt-Eickschen and O'Neill (2005)), the amount of Ti is at
991 the upper end of natural concentrations (De Hoog et al., 2010). Figure 17 shows
992 that the creep strength in diffusion creep is somewhat below that of undoped
993 solgel Faul and Jackson (2007), although the Ca-doped samples are essentially
994 within the uncertainties of the fit using the parameters of the undoped samples.
995 The Ti-doped samples, deformed in $Ni_{70}Fe_{30}$ foil show no detectable water after
996 the experiments (Faul et al., 2016) and are systematically weaker. Uncertainties
997 in rheological data result from possible temperature gradients as well as from the
998 limited accuracy of grain size determination. The strain rate is very sensitive to
999 grain size ($\propto d^3$).

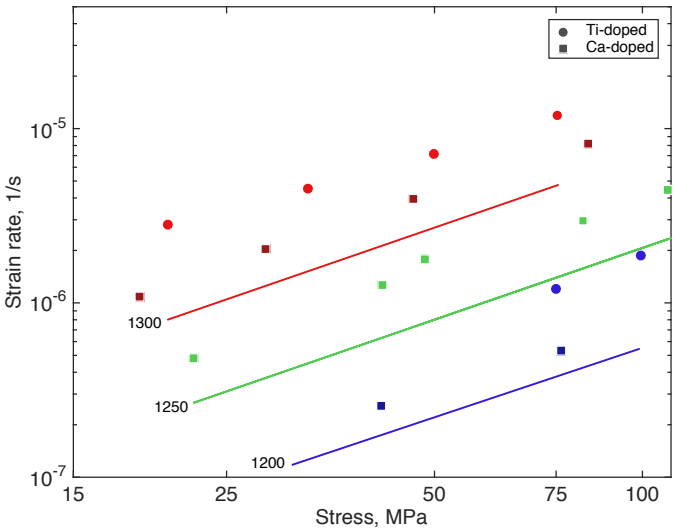

Fig. 17 Diffusion creep strain rates of melt-free solgel olivine doped with $0.15wt\%$ CaO (squares) and Ti (dots, see Table 1). The data are plotted at the experimental temperatures, normalised to 5 μm grain size. Temperatures in °C are indicated next to the fit to the data from undoped solgel from Faul and Jackson (e.g. 2007, (lines)). Overall the doped samples appear slightly weaker compared to the undoped polycrystals. The amount of Ca dopant is similar to that found in olivine from relatively fertile peridotite xenoliths (Witt-Eickschen and O'Neill (2005))

5 Discussion

The GBCD of Ti doped but otherwise pure Fo_{90} sol-gel shown in Figure 5 can be compared to the Al bearing forsterite examined in Marquardt et al. (2015). In the forsterite a-planes dominate, followed by b and c-planes. By contrast, the habit of the sol-gel Fo_{90} sample (Figure 5) is dominated by c-planes. This is agreement with previous, non-quantitative observations by Miyazaki et al. (2013). Our quantitative measurements support their conjecture that chemical composition has an effect on the equilibrium crystal habit. A consideration for the GBP/GBCD is that SEM observations show that individual grain boundaries, especially of grains larger than a few μm are often curved and are thus formed by several differently oriented grain boundary planes, as indicated in the scheme of Figure 2 and for example the SEM images in Garapic et al. (2013); Miyazaki et al. (2013); Mu and Faul (2016).

Grain boundary plane distributions, analogous to steady state grain size distributions, have been shown to be self-similar (e.g. Rohrer, 2007). Deformation probably affect the GBPD, depending on the texture dominating mechanism, for example surface energy minimisation vs. dislocation glide resulting in many low angle (high energy) grain boundaries. The grain boundary structure (the width of the apparently amorphous region between two adjacent grains) can also be compared for different sample types. High resolution transmission electron microscopic images of synthetic, nearly melt-free natural, or melt-added natural and synthetic samples all appear to have a similar grain boundary width at the scale considered (section 4.2). Hiraga et al. (2002) also show that melt-free grain boundaries in partially molten samples are indistinguishable from grain boundaries in melt-free samples. This is largely in agreement with the grain boundary width obtained using molecular dynamic simulations, where widths ranging from less than 0.5 nm to about 2 nm are obtained (Wagner et al., 2016; Mantisi et al., 2017). The structural width of grain boundaries (not the structure) is insensitive to sample origin, trace element content or the presence of a melt in the sample. The analyses of olivine grain boundaries presented here as well as in the literature (for example Tan et al.,

2001; Hiraga et al., 2003) indicate that the width of the trace element-enriched boundary region is similar to the imaged structural width. Molecular dynamics simulations of self-diffusion similarly imply a grain boundary width of about 1 nm (Wagner et al., 2016). These findings raise the question whether it is justified to invoke an 'effective' grain boundary width that is significantly wider than the 'structural' width to explain experimental observations related to diffusion.

An actual challenge using TEM is that this method does not succeed to sample representative numbers of grain boundaries. When differentiating grain boundary orientations at 10° angular resolution more than 60.000 orientations can be differentiated in the orthorhombic crystal system. This number, while being a conservative estimate, indicates not only the limitations of TEM but also of molecular dynamic simulations that use a infinite continuum of grains while sampling only orientation between few grains (Mantisi et al., 2017, 10 grains).

As discussed in section 3 (Methods), the use of small objective apertures in earlier work allowed resolution of only the largest interplanar spacings. This may give the impression that a grain boundary is facetted because d-spacings with large d, that have been imaged is the presented cases, meet the grain boundary at an angle <90°. However, if also higher frequencies are allowed to contribute to image formation and smaller d-spacings are simultaneously imaged, the interface would appear straight (Figure 7). The TEM micrographs therefore show that olivine grain boundaries are mainly smooth at scales of nm, with some facets with dimensions of tens of nm.

By contrast, steps at a scale smaller than the unit cell (sub nm) seem to be relatively common (e.g. Figure 7 and the micrographs published in Figure 1 of Fei et al. (2016) and Figure 4b in Hiraga et al. (2002)). It is likely, that the steps size is determined by the the size of one formula-unit of olivine ($\sim \frac{1}{4}$ of the unit cell) to maintain charge neutrality. Such a constraint seems plausible, because in olivine neither evaporation (personal communication, S. Chakraborty) nor silicification (King et al., 2011) does lead to a surface layer with compositional changes. This

is indicative of the addition/removal of elements in portions of complete formula units. This interpretation contrasts with findings that are interpreted as more supportive of leaching of individual ions or components rather than formula units (e.g. Casey et al., 1993; Oleg and Jacques, 2007; Morrow et al., 2010; Maher et al., 2016).

The most extreme examples of facetted and stepped grain boundaries were presented by Vaughan et al. (1982), but have been interpreted as non-equilibrium states, in agreement with the theoretical treatment by Raj and Ashby (1971). Raj and Ashby (1971) argue that steps at small scales should become smooth quickly through diffusive material redistribution.

The bicrystal grain boundary produced by wafer bonding consists of (011) planes of the two crystals with a 60.8° rotation about the common [100] axis. The same grain boundary geometry was simulated by Adjaoud et al. (2012); Wagner et al. (2016) and Cordier et al. (2014), and has been discussed by Faul and Fitz Gerald (1999) as a grain boundary more frequently melt-free in partially molten samples (their Figure 5) than other interfaces. This particular axis/angle combination ([100]/60) is indeed favourable for (011) planes, as quantified in the GBPD in Figure 5d. Marquardt et al. (2015) also found this grain boundary to occur with high frequency, implying a minimum energy configuration. The (011) planes of both adjacent crystals are in contact by a 60.8° rotation about the common [100] axis. This particular grain boundary might prove to be the exception to the rule, and represent a structurally special grain boundary with a special characteristic, namely low energy. It remains to be proven, that 60 pseudo symmetric misorientations are well cleaned using EBSD cleaning procedures. If we assume the cleaning is sufficiently good, our statistics indicate, that among the misorientations of 60°, that have random frequencies this particular grain boundary contributes most grain boundary orientations. If the presence of such grain boundaries, with the indicated occurrence probabilities affect for example contiguity requires the testing using anisotropic microstructure models.

TEM micrographs indicate that the structural grain boundary width, δ_{struc} is about 1 nm. This is true for 'amorphous appearing' grain boundaries shown in Figure 6, 7, 8 as well as disordered or 'crystalline appearing' grain boundaries (Figure 6, 9, 10), which only appear different as a result of the imaging technique. Both types of grain boundaries are distinct from those that contain a thin layer of glass. Grain boundaries with a glass layer of 1-2 nm were described by Wirth (1996) from grain boundaries in a xenolith, but processes during entrainment and eruption may have modified the boundaries. Faul and Fitz Gerald (1999) define melt (glass) layers as being parallel-sided and thicker than 5 nm to distinguish them from films observed in silicon-nitride (Clarke, 1979b) with a width of 1 - 2 nm. Glass layers with a width of 10 nm were described as lower limit in TEM images from experimental samples (Cmíral et al., 1998). In contrast to the current description of grain boundaries with a width of 1 nm Cmíral et al. (1998) referred to trace element enriched grain boundary as films, following Drury and Fitz Gerald (1996). A minimum glass layer thickness of about 10 nm is consistent with observations from Vaughan et al. (1982, Figure 7b) and Hiraga et al. (2002, Figure 6). Hiraga et al. (2002, Figure 7) shows a very small dihedral angle, distinct from a parallel-sided layer.

Although very few olivine-enstatite phase boundaries have been imaged at high resolution, the example in Figure 11 and Figure 6 seem to indicate that these boundaries are very dense. Such micrographs unfortunately do not allow to evaluate how effective processes, such as grain boundary diffusion and associated properties such as diffusion creep or attenuation of seismic waves are.

The shape of the interface phase that precipitated in the Ti-oversaturated systems can be used to infer relative surface energies 1.5. Their shape depends on whether the phase occurs on enstatite olivine phase boundaries, or at olivine grain boundaries. The precipitates formed at the olivine grain boundaries show a comparable dihedral angles on both surfaces, Figure 13. This indicates that the olivine surface in contact have similar energies as well. At enstatite-olivine phase

boundaries the interface phase is flat towards olivine, but curved towards enstatite (Figure 12). Because surfaces with higher energy have higher wettabilities, the observation indicates that the surface energy of olivine is higher than that of enstatite. This conclusion is in agreement with the wetting relation observed by Schäfer and Foley (2002). They found that wetting decreases in the order forsterite, diopside, enstatite, and spinel, indicating a corresponding order of surface energies, with forsterite having the highest.

The trace element content in olivine grain boundaries is determined by the bulk composition of the aggregate. San Carlos olivine is comparatively depleted, and correspondingly contains low concentration of trace elements at grain boundaries in samples without added melt. After equilibration with a basaltic melt, both grain interiors and grain boundaries contain significantly higher trace element concentrations. A relationship between grain boundary and grain interior composition was previously noted by Hiraga et al. (2004). Support for equilibration of grain boundaries with grain interiors comes from the observation that neoblast boundaries (formed during deformation) are relatively trace element poor, but revert to higher concentrations after annealing (Figure 16). Grain boundaries may therefore constitute a separate phase in the sense of Gibbs.

Trace elements that have elevated concentrations in grain boundaries are Ca, Al, Ti, Cr Mn and Co, while Ni as the most abundant compatible trace elements in olivine interiors is not elevated in grain boundaries (c.f. Hiraga et al., 2003). In contrast to the full solid solution with Ni, Cr^{2+} substitution is limited to a maximum of $\sim 25\ mol-\%$ (Miletich et al., 1999). For natural olivine, a complete solid solution between forsterite, Mg_2SiO_4 and fayalite, Fe_2SiO_4 can take only a few mole% of Ca, and does not completely mix with the second complete solid solution between monticellite, $CaMgSiO_4$ and krichsteinite, $CaFeSiO_4$ (Brown, 1980). The second solid solution has a markedly larger unit cell, caused by the larger ionic radius of Ca compared to Mg and Fe ($Ca^{[6]}114pm$, $Mg^{2+[6]}$ $86pm$, $Fe^{2+[6]}$ $92pm$, $Fe^{3+[6]}$ $78.5pm$). Finally, also solid solutions with the Co and Mg

endmembers exist (Seifert and O'Neill, 1986). In addition to the bulk composition, olivine grain boundary composition is therefore influenced by crystal chemical considerations.

6 Inferences from Physical Properties

Experimentally determined physical properties that are likely dependent on grain boundary structure and properties are discussed in the following, with consideration of the observations presented above.

In ceramics, the most commonly observed effect of trace elements on grain boundary diffusion is to decrease diffusivities. Properties such as grain growth rates, seismic velocities and attenuation, as well as diffusion creep all have grain boundary diffusion as an underlying process. The prediction of decreased diffusivity in impure ceramics systems can therefore be compared with experimental observations, which are discussed in the following.

Seismic properties have been measured using samples of trace element-containing, reconstituted natural-origin olivine (Figures 15 and 16), as well as trace element-free and Ti-doped solution-gelation-derived olivine. No measurable systematic differences between these different samples types have been detected, as long as other variables such as melt and capsule material are accounted for (Faul and Jackson, 2005; Jackson and Faul 2010; Jackson, 2015). At least for grain boundary diffusion as implicated in models of diffusionally assisted grain boundary sliding (Section 1.7.2) trace elements seem not to affect sample-averaged diffusivities of Fe-bearing olivine. However the properties of iron free systems vary markedly.

Inferring grain boundary diffusivities from grain growth rates is problematic since a number of processes can contribute to the observed rate. Examples of processes that do not depend on diffusion along the grain boundary are grain boundary migration Karato (1989), and coalescence of grains (e.g. Figure 2a of Faul et al., 2016). As discussed for example by Ricoult and Kohlstedt (1983), care

needs to be taken to separate diffusion along a stationary grain boundary from simultaneous grain growth (diffusion across a grain boundary, Peterson (1983)).

At least solgel olivine (Fo_{90}) doped with Ca or Ti show no variation of grain growth rates compared to undoped system. Solgel olivine doped with 0.15 wt. % Ca has mean grain sizes that are comparable to undoped solgel for the same hot pressing temperature (3 - 3.3μm, Table1 compared to 2.7 - 4.3 μm, samples 6533, 6536, 6580 of Faul and Jackson (2007)). Ti-doped samples hotpressed at 1300°C again have similar mean grain sizes as undoped samples hotpressed at this temperature (5.5 - 5.6 μm, Table1 compared to 3.6 - 5.4 μm; samples 6508, 6518, 6512, 6522, 6525 of Faul and Jackson (2007)). Figures 14, 15 and 16 confirm that Ti or Ca are enriched in grain boundaries where these elements are present in the bulk samples. Growth rates of San Carlos olivine containing a broad range of trace elements have grain sizes at the upper end of undoped solgel olivine, although a more comprehensive comparison is complicated by the difficulty in producing melt-free aggregates.

Together these observations suggest that trace elements do not substantially modify grain growth rates at otherwise identical conditions. The concept of impurity drag (incompatible elements in grain boundaries slowing growth rates by effectively pinning the boundary, (Peterson, 1983)) therefore does not seem to apply to olivine. As described above, the structural width of grain boundaries observed in HRTEM images is not significantly sensitive to impurity content.

For diffusion creep, impurities in ceramics have been observed to decrease diffusivities with a consequent increase in strength (e.g. Yasuda et al., 2004). For olivine, when the effect of melt is accounted for Hirth and Kohlstedt (1995); Faul and Jackson (2007), again no systematic effect of trace elements on rheology is observable. Figure 17 shows that doping of Fo_{90} solgel with Ca marginally decreases the strength, although the difference to the undoped flow law of Faul and Jackson (2007) is within the experimental and analytical uncertainty. Doping with Ti decreases the strength somewhat more (dry conditions, Faul et al., 2016).

Together with the reanalysis of the grain size of Hirth and Kohlstedt (1995) performed by Hansen et al. (2011) this reduces the difference in strain rate between olivine reconstituted from natural rocks and solgel olivine to about one order of magnitude, consistent with the predictions of the effect of melt on rheology by the model of Takei and Holtzman (2009a). At this point we infer that similar to seismic properties and grain growth the averaged grain boundary diffusivity for Fe-bearing olivine implied by the deformation experiments is not substantially affected by the presence of trace elements.

Overall, experiments on Fe-bearing polycrystalline olivine show an insensitivity of physical properties to the trace element compositions of grain interiors and grain boundaries. This statement applies provided that all other conditions are the same, i.e. the presence or absence of melt, capsule material/oxygen fugacity, and the presence or absence of water. HRTEM images of grain boundaries similarly show no relationship between grain boundary width and the presence or concentration of trace elements. The apparent rarity of steps in HRTEM images as discussed above is in agreement with the scaling of diffusionally assisted grain boundary sliding with the (mean) grain size.

The absence of an apparent effect of trace elements on diffusive properties does no preclude differences in structure and properties between different grain boundaries in the five parameter orientation space. An indication that grain boundary properties are dependent on the orientation of the neighbouring grains and the grain boundary plane orientation is evident from the axis/angle distribution distribution (Figure 5b) in combination with the grain boundary plane distribution of planes misoriented by about 60 around the a-axis (Figure 5d). The frequency distribution of misorientation axes has a maximum near [100] for disorientation angles near 60°. Faul and Fitz Gerald (1999) found that in melt-bearing polycrystalline olivine grain boundaries with this disorientation angle were preferentially melt-free. This suggests that this type of grain boundary has a lower energy in comparison to other general, high angle grain boundaries.

Pre-melting at grain boundaries is predicted to produce nanometer-scale intergranular films with liquid-like properties significantly below the bulk melting temperature (Section 1.4). A complication for the application of the concept of pre-melting to rocks is that their bulk melting temperature is dependent on composition, and may vary up to 600 K between a dunite and a fertile, volatile-bearing lherzolite.

HRTEM observations from samples hot-pressed at the same temperature, both melt-free and melt-bearing, show no films or layers between 1 and about 10 nm in width. Melt films <1 nm in width (i.e. less than the largest unit cell dimension) would be dominated by surface forces and therefore not have properties in between melt and grain boundary properties. Similarly, attenuation and deformation experiments correlate with the presence of melt identifiable by high resolution SEM imaging (i.e. melt layers to $\sim$10 nm), but do not show softening where melt can not be identified by SEM or TEM.

7 Conclusions

In conclusion, high resolution, edge-on TEM images of general grain boundaries in olivine show that their structural width is about 1 nm, independent of the origin of the sample material and the composition of olivine grain interiors and hence bulk composition. Depending on imaging conditions the observations of amorphous appearing interfaces (Faul et al., 2004, and others) or the crystalline appearance (e.g. Hiraga et al., 2002) can be reproduced on the same grain boundary 6a-d. Furthermore, both image types where also produced on vacuum sintered samples (Fei et al., 2016). Therefore differing grain boundary structures are due to different TEM imaging conditions and techniques, including image delocalization, which lowers the interpretable resolution Due to the large number of geometrically distinguishable grain boundaries TEM will currently not succeed to sample a representative number of interfaces (see section 5). The grain boundary composition varies with bulk composition, consistent with the observations of Hiraga et al. (2003). Nevertheless, there is growing evidence that the concentration of incompatible elements in

grain boundaries changes the grain boundary plane distribution and consequently the grain boundary energy, which is not observable in HRTEM micrographs of individual boundaries. In the absence of spherical aberration corrected HRTEM micrographs it is not possible to answer the question of how narrow a film of melt (or 'melt-like structure') can be, but still be clearly distinguishable from an 'amorphous' type boundary, which is disordered but melt-free.

We conclude this contribution with a summation of observations:

(i) Only a limited number of direct grain boundary observations are available today, their entirety is only a small fraction of the full geometric parameter space available (100 out of 60.000, see section 5. Consequently grain boundary geometries and structures and their relation to properties are still relatively poorly characterised.

(ii) The GBCD circumvents the problem of small numbers of observations by HRTEM, and associated human bias of generalising from the particular (see the illustrative examples given by Tversky and Kahneman (1974); Kahneman and Tversky (1981)).

(iii) No melt layers $< 10\ nm$ have been observed by HRTEM. 'Amorphous' and 'crystalline' appearing boundaries have a width of 1 nm or less with properties intermediate between grain interiors and melt and varying for different grain boundary planes (Maruyama and Hiraga, 2017b,a).

(iv) Theoretically, grain boundary segregation should cause a decrease in diffusive properties, but the experimental evidence from polycrystalline olivine currently does not support this notion.

(v) For a specific rotation axis orientation, the transition from low to high angle grain boundaries in olivine is at $\sim 20^\circ$ as shown by experiments and computations (Heinemann et al., 2005; Adjaoud et al., 2012).

These observations result in the following hypothesis that seem viable at this point of research, but need further work to substantiate them:

1. GBPD of olivine is directly linked to grain boundary properties. These in turn influence bulk rock behaviour.
2. GBPD may change due to small fractions of melt, and/or as a function of contiguity and composition of the melt.
3. Spherical aberration corrected HRTEM micrographs on statistically representative grain boundaries are necessary to link atomic structure to macroscopic properties.
4. A physical description of atomic scale processes at grain boundaries during grain boundary migration and grain growth are desirable.
5. Material science observations and models predict that grain boundary segregations should cause a change in the GBPD and a change in grain boundary diffusivity. The influence of grain boundary composition on the behaviour of polycrystalline olivine and more generally rocks needs to be further explored.

8 Appendix

8.1 Nomenclature & definitions

Interface: Where two media are in contact we speak of an interface. This term encompasses, solid - liquid, solid - gaseous, gaseous - liquid contacts as well as solid - solid, gas-gas, or liquid - liquid contact zones. Both grain and phase boundaries are interfaces.

Phase boundary: Phase boundaries are interfaces between two different solid phases, generally minerals.

Grain boundary: The grain boundary defines the interface where two minerals of the same phase are in contact. The only characteristic that varies between the two grains (crystals) is the orientation of the crystal lattice. The grain boundary it self needs five macroscopic parameters for its macroscopic geometry description.

Triple junction/line: Three grains of one phase meet to form a line in 3D-space and a point in a 2D section, when interfacial energies are approximately equal this triple junction has 120° angles, typical for soap foam.

Quadrupole junction: four grains of the same phase meet in a nod (Chaim (1997)).

Grain boundary structure: The atomic configuration that is repetitive along the grain boundary. Different geometric models have been developed to describe grain boundary structures.

Coincidence side lattice model (CSL): Probably the most successful geometric model that yields the density of coinciding lattice points of two super imposed adjacent crystal lattices. The inverse of coinciding number of lattice sides, n, yields the Σ-value: $\Sigma = 1/n$.

Grain boundary character distribution (GBCD): The distribution of the grain boundary geometries in their five parameter space for a polycrystalline sample can be described by the GBCD (Watanabe, 1983, 1979; Watanabe et al., 1989).

Grain boundary energy: The grain boundary energy is an anisotropic property of grain boundaries (e.g. Smith, 1948). The anisotropy arrises from the different structures of the grain boundaries at the nm-atomic-scale.

Grain boundary width: The grain boundary width is a controversial term, that encompasses the structural grain boundary width (Clarke, 1979a), but also includes the effective grain boundary width for various processes that can be orders of magnitude larger.

Grain boundary segregation: grain boundaries are preferential sites for segregation of impurities and elements incompatible in the perfect crystal lattice. This results in a thin layer with a chemical composition that differs from the crystal volume. The creep resistance of several non-geological materials generally increase significantly due to grain boundary segregation (Cho et al., 1999; Yasuda et al., 2004; Milas et al., 2008; Harmer, 2010), in rare cases also decreases (Yasuda et al., 2004). Segregation can cause variation of electrical conductivity for example its enhancement in the case of proton doping (Shirpour et al., 2012).

Grain boundary layer & film: The terms have been coerced by Clarke in several publications (Clarke, 1979a,b, 1987). Film refers to the existence of a chemically and structurally distinct film fully covering all grain boundaries in ceramics. It is noticeable that such films have a wetting angle of 0° and are thermodynamically stable.

Grain boundary layer: differs from the film as its properties are much less defined and less well understood and do not meet the full wetting criterion.The term grain boundary layer is used to refer to the chemically and structurally distinct region of the grain boundary, that results from the mismatch of the adjacent crystals, segregation of impurities or incompatible elements.

Grain boundary pre-melting: pre-melting is a phenomenon where a thin region at the grain boundary melts at a temperature below the bulk melting temperature, or the bulk eutectic (melting) temperature. Experimentally this has been shown

for ice, Pb, W doped with Ni and other unary systems, and is reviewed in several articles (Luo and Chiang, 2008; Mellenthin et al., 2008).

Complexion: Grain boundary films and layers can often be regarded as interface stabilised phases that are thermodynamically stable and have distinct structural and chemical properties with temperature (Kelly et al., 2016) and pressure dependent transitions. These interface-stabilised phases are called complexions. In recent years grain boundary complexions gained more and more interest in material sciences (Rohrer, 2011b; Bojarski, 2014). However in geology, complexions have not yet been described as general grain boundary features; might however occur and if we interpret the term widely they encompass quasi-crystalline materials which are treated as interface phenomena theoretically by Romeu (Romeu, 2003) have been observed associated to olivine in Khatyrka meteorite (Bindi et al., 2015) however not explicitly as interface phase. Note, that complexions may not be of first order importance as geological relevant materials are usually chemically highly complex, probably inhibiting the formation of complexions or resulting in such a high variability of complexions that their identification and study might prove difficult or impossible. For the sake of completeness we like the reader to note that complexions have been shown to affect grain growth (Dillon et al., 2010) as well as sintering behaviour (Luo and Chiang, 2008; Luo, 2012).

Note, that some of the above terms are partially interchangeable and have evolved during the years. The literature of interfaces, grain - and phase boundaries tries to categorise a subject with fluent boundaries, thus the nomenclature is partially fluent as well.

Acknowledgments We gratefully acknowledge discussions with our colleagues John Fitz Gerald, Ian Jackson and Chris Cline as well as Hauke Marquardt and Nobuyoshi Miyajima. We are also grateful for the technical support at ANU (Harri Kokkonen, Hayden Miller) and BGI (Hubert Schulz, Raphael Njul). U.F. acknowledges support from NSF grant EAR-1321889 and EAR-1464024. KM acknowledges support from the German Science Foundation (MA6287/3, MA6287/6). The FEI Scios FIB machine at BGI Bayreuth is supported through grant INST 91/315-1 FUGG. We are grateful to Sylvie Demouchy and one anonymous reviewer for their meticulous and thorough reviews. Any surviving errors of omission or commission are entirely ours.

References

Adams, B. L., Ta'asan, S., Kinderlehrer, D., Livshits, I., Mason, D. E., Wu, C.-T., Mullins, W. W., Rohrer, G. S., Rollett, A. D., and Saylor, D. M. (1999). Extracting grain boundary and surface energy from measurement of triple junction geometry. *Interface Science*, pages 321–338.

Adams, B. L., Wright, S. I., and Kunze, K. (1993). Orientation imaging: The emergence of a new microscopy. *Metallurgical Transactions A*, 24(4):819–831.

Adjaoud, O., Marquardt, K., and Jahn, S. (2012). Atomic structures and energies of grain boundaries in Mg2SiO4 forsterite from atomistic modeling. *Physics and Chemistry of Minerals*, 39(9):749–760.

Alsayed, A. M., Islam, J. F., Zhang, J., Collings, P. J., and Yodh, A. (2005). Premelting at Defects Within Bulk Colloidal Crystals. *Science*, 309(August):1207–1210.

Anderson, D. L. and Sammis, C. (1970). Partial melting in the upper mantle. *Physics of the Earth and Planetary Interiors*, 3:41–50.

Armstrong, J. (1995). CITZAF: A package of correction programs for the quantitative electron microbeam X-ray-analysis of thick polished materials, thin films, and particles. *Microbeam Anal.*, 4:177–200.

Ashby, M. (1972). Boundary defects, and atomistic aspects of boundary sliding and diffusional creep. *Surface Science*, 31:498–542.

1405 Ashby, M. F., Raj, R., and Gifkins, R. C. (1970). Diffusion-controlled sliding at a
1406 serraed grain boundary. *Scripta Metallurgica*, 4:737–742.

1407 Avramov, I. (2009). Relationship between diffusion, self-diffusion and viscosity.
1408 *Journal of Non-Crystalline Solids*, 355(10-12):745–747.

1409 B. Fultz, J. H. (2001). *Transmission Electron Microscopy and Diffractometry of*
1410 *Materials*. Springer-Verlag Berline Heidelberg.

1411 Bagdassarov, N., Laporte, D., and Thompson, A. B. (2000). *Physics and Chemistry*
1412 *of Partially Molten Rocks*. Kluwer Academic Publishers.

1413 Bean, J. J. and McKenna, K. P. (2016). Origin of differences in the excess volume
1414 of copper and nickel grain boundaries. *Acta Materialia*, 110:246–257.

1415 Beeman, M. L. and Kohlstedt, D. L. (1993). Deformation of fine-grained aggregates
1416 of olivine plus melt at high temperatures and pressures. *Journal of Geophysical*
1417 *Research*, v. 98(no. B4):p. 6443–6452.

1418 Bhogireddy, V. S. P. K., Hüter, C., Neugebauer, J., Steinbach, I., Karma, A., and
1419 Spatschek, R. (2014). Phase-field modeling of grain-boundary premelting using
1420 obstacle potentials. *Physical Review E - Statistical, Nonlinear, and Soft Matter*
1421 *Physics*, 90(1):1–10.

1422 Bindi, L., Yao, N., Lin, C., Hollister, L. S., Andronicos, C. L., Distler, V. V.,
1423 Eddy, M. P., Kostin, A., Kryachko, V., MacPherson, G. J., Steinhardt, W. M.,
1424 Yudovskaya, M., and Steinhardt, P. J. (2015). Natural quasicrystal with
1425 decagonal symmetry. *Scientific Reports*, 5:9111.

1426 Bojarski, S. A. (2014). The Effects of Grain Boundary Character and Energy on
1427 Complexion Transitions in Ceramics. page 156.

1428 Boneh, Y., Wallis, D., Hansen, L. N., Krawczynski, M. J., and Skemer, P. (2017).
1429 Oriented grain growth and modification of frozen anisotropy' in the lithospheric
1430 mantle. *Earth and Planetary Science Letters*, 474:368–374.

1431 Brown, G. E. (1980). ORTHOSILICATES. In Ribbe, P. H., editor, *Reviews in*
1432 *Mineralogy*, volume 5, chapter 11 Olivine, pages 275–365.

Bruno, M., Massaro, F. R., Prencipe, M., Demichelis, R., De La Pierre, M., and Nestola, F. (2014). Ab Initio Calculations of the Main Crystal Surfaces of Forsterite (Mg2SiO4): A Preliminary Study to Understand the Nature of Geochemical Processes at the Olivine Interface. *The Journal of Physical Chemistry C*, 118:2498–2506.

Bruno, M., Rubbo, M., Aquilano, D., Massaro, F. R., and Nestola, F. (2016). Diamond and its olivine inclusions: A strange relation revealed by ab initio simulations. *Earth and Planetary Science Letters*, 435:31–35.

Bulau, J. R., Waff, H. S., and Tyburczy, J. A. (1979). Mechanical and thermodynamical constraints on fluid distribution in partial melts. *Journal of Geophysical Research*, 84(9).

Burke, J. and Turnbull, D. (1952). Recrystallization and grain growth. *Progress in Metal Physics*, 3:220–292.

Burnard, P. G., Demouchy, S., Delon, R., Arnaud, N. O., Marrocchi, Y., Cordier, P., and Addad, A. (2015). The role of grain boundaries in the storage and transport of noble gases in the mantle. *Earth and Planetary Science Letters*, 430:260–270.

Cabane, H., Laporte, D., and Provost, A. (2005). An experimental study of Ostwald ripening of olivine and plagioclase in silicate melts: implications for the growth and size of crystals in magmas. *Contributions to Mineralogy and Petrology*, 150(1):37–53.

Cahn, J. W., Mishin, Y., and Suzuki, A. (2006). Coupling grain boundary motion to shear deformation. *Acta Materialia*, 54(19):4953–4975.

Casey, W. H., Westrich, H. R., Banfield, J. F., Ferruzzi, G., and Arnold, G. W. (1993). Leaching and reconstruction at the surfaces of dissolving chain-silicate minerals. *Nature*, 366(6452):253–256.

Chaim, R. (1997). Percolative composite model for prediction of the properties of nanocrystalline materials. *Journal of Materials Research*, 12(07):1828–1836.

Chakraborty, S. (1997). Rates and mechanisms of Fe-Mg interdiffusion in olivine at 980-1300C. *Journal of Geophysical Research: Solid Earth*, 102(B6):12317–12331.

Chakraborty, S., Farver, J. R., Yund, R. A., Rubie, D. C., Miherais, I., and Chakrahorty, S. (1994). Mg tracer diffusion in synthetic forsterite and San Carlos Olivine as a function of P, T and fO (sub 2). *Physics and Chemistry of Minerals*, 21(8):489–500.

Chan, S. W. and Balluffi, R. W. (1986). Study of energy vs misorientation for grain boundaries in gold by crystallite rotation method-II. Tilt boundaries and mixed boundaries. *Acta Metallurgica*, 34(11):2191–2199.

Ching, W. Y. and Xu, Y.-N. (1999). Nonscalability and nontransferability in the electronic properties of the Y-Al-O system. *Physical Review B*, 59(20):12815.

Cho, J., Wang, C. M., Chan, H. M., Rickman, J. M., and Harmer, M. P. (1999). Role of segregating dopants on the improved creep resistance of aluminum oxide. *Acta Materialia*, 47(15-16):4197–4207.

Cinibulk, M. K., Kleebe, H.-j., and Ruhle, M. (1993). Quantitative Comparison of TEM Techniques for Determining Amorphous Intergranular Film Thickness. *Journal of the American Ceramic Society*, 76(2):426–432.

Clarke, D. R. (1979a). High-Resolution Techniques and Application to Nonoxide Ceramics. *Journal of the American Ceramic Society*, 62(5-6):236–246.

Clarke, D. R. (1979b). On the detection of thin intergranular films by electron microscopy. *Ultramicroscopy*, 4(1):33–44.

Clarke, D. R. (1987). On the Equilibrium Thickness of Intergranular Glass Phases in Ceramic Materials. *Journal of the American Ceramic Society*, 70(1):15–22.

Cmíral, M., Fitz Gerald, J. D., Faul, U. H., and Green, D. H. (1998). A close look at dihedral angles and melt geometry in olivine-basalt aggregates: a TEM study. *Contributions to Mineralogy and Petrology*, 130(3-4):336–345.

Cooper, R. and Kohlstedt, D. (1982). Interfacial energies in the olivine basalt system. In Akimoto, S. and Manghnani, M., editors, *High-pressure research in geophysics*, pages 217–228. Reidel, with Center for Academic Publications

Japan; AEPS 12.

Cooper, R. and Kohlstedt, D. (1984). Solution-precipitation enhanced diffusional creep of partially molten olivine-basalt aggregates during hot-pressing. *Tectonophysics*, 107(3-4):207–233.

Cordier, P., Demouchy, S., Beausir, B., Taupin, V., Barou, F., and Fressengeas, C. (2014). Disclinations provide the missing mechanism for deforming olivine-rich rocks in the mantle. *Nature*, 507:51–56.

Czochralski, J. (1918). Ein neues Verfahren zur Messung der Kristallisationsgeschwindigkeit der Metalle. *Zeitschrift für physikalische Chemie*, 92:219–221.

Dai, L., Li, H., Hu, H., and Shan, S. (2008). Experimental study of grain boundary electrical conductivities of dry synthetic peridotite under high-temperature, high-pressure, and different oxygen fugacity conditions. *Journal of Geophysical Research*, 113(B12):B12211.

Dash, J. G. (1999). RMP Colloquia History of the search for continuous melting. *Review of Modern Physics*, 71(5):1737–1743.

Davies, G. R., Stolz, A. J., Mahotkin, I. L., Nowell, G. M., and Pearson, D. G. (2006). Trace element and Sr-Pb-Nd-Hf isotope evidence for ancient, fluid-dominated enrichment of the source of Aldan Shield lamproites. *Journal of Petrology*, 47(6):1119–1146.

De Hoog, J. C., Gall, L., and Cornell, D. H. (2010). Trace-element geochemistry of mantle olivine and application to mantle petrogenesis and geothermobarometry. *Chemical Geology*, 270(1-4):196–215.

de Kloe, R. (2001). Deformation mechanisms and melt nano-structures in experimentally deformed olivine-orthopyroxene rocks with low melt fractions. *Thesis*, (201):176.

De Kloe, R., Drury, M. R., and van Roermund, H. L. M. (2000). Evidence for stable grain boundary melt films in experimentally deformed olivine-orthopyroxene rocks. *Physics and Chemistry of Minerals*, 27:480–494.

de Leeuw, N. H., Catlow, C. R. a., King, H. E., Putnis, A., Muralidharan, K., Deymier, P., Stimpfl, M., and Drake, M. J. (2010). Where on Earth has our water come from? *Chemical communications (Cambridge, England)*, 46(47):8923–8925.

de Leeuw, N. H., Parker, S. C., Catlow, C. R. a., and Price, G. D. (2000a). Modelling the effect of water on the surface structure and stability of forsterite. *Physics and Chemistry of Minerals*, 27(5):332–341.

de Leeuw, N. H., Parker, S. C., Catlow, C. R. A., and Price, G. D. (2000b). Proton-containing defects at forsterite {010} tilt grain boundaries and stepped surfaces. *American Mineralogist*, 85(9):1143–1154.

Demouchy, S. (2010). Diffusion of hydrogen in olivine grain boundaries and implications for the survival of water-rich zones in the Earth's mantle. *Earth and Planetary Science Letters*, 295(1-2):305–313.

Dillon, S. J. and Harmer, M. P. (2007). Multiple grain boundary transitions in ceramics: A case study of alumina. *Acta Materialia*, 55(15):5247–5254.

Dillon, S. J., Harmer, M. P., and Rohrer, G. S. (2010). The Relative Energies of Normally and Abnormally Growing Grain Boundaries in Alumina Displaying Different Complexions. *Journal of the American Ceramic Society*, 1802:1796–1802.

Dohmen, R. and Milke, R. (2010). Diffusion in Polycrystalline Materials: Grain Boundaries, Mathematical Models, and Experimental Data. *Reviews in Mineralogy and Geochemistry*, 72(1):921–970.

Doukhan, N., Doukhan, J. C., Ingrin, J., Jaoul, O., and Raterron, P. (1993). Early partial melting in pyroxenes. *American Mineralogist*, 78(11-12):1246–1256.

Drouin, M., Godard, M., Ildefonse, B., Bruguier, O., and Garrido, C. J. (2009). Geochemical and petrographic evidence for magmatic impregnation in the oceanic lithosphere at Atlantis Massif, Mid-Atlantic Ridge (IODP Hole U1309D, 30N). *Chemical Geology*, 264(1-4):71–88.

1547 Drury, M. R. (2005). Dynamic recrystallization and strain softening of olivine
1548 aggregates in the laboratory and the lithosphere. *Geological Society London*
1549 *Special Publications*, 243(2):143–158.

1550 Drury, M. R. and Fitz Gerald, J. D. (1996). Grain boundary melt films in
1551 an experimentally deformed olivine-orthopyroxene rock: Implications for melt
1552 distribution in upper mantle rocks. *Geophysical Research Letters*, 23(7):701–
1553 704.

1554 Drury, M. R. and Urai, J. L. (1990). Deformation-related recrystallization
1555 processes.

1556 Durham, W. B. and Goetze, C. (1977). Plastic flow of oriented single crystals of
1557 olivine: 1. Mechanical data. *Journal of Geophysical Research*, 82(36):5737–5753.

1558 Durham, W. B., Goetze, C., and Blake, B. (1977). Plastic flow of oriented
1559 single crystals of olivine: 2. Observations and interpretations of the dislocation
1560 structures. *Journal of Geophysical Research*, 82(36):5755–5770.

1561 Duyster, J. and Stöckhert, B. (2001). Grain boundary energies in olivine derived
1562 from natural microstructures. *Contributions to Mineralogy and Petrology*,
1563 140(5):567–576.

1564 Edgar, A. D. (1973). *Experimental Petrology*. Clarendon Press.

1565 Eggins, S., Rudnick, R., and McDonough, W. (1998). The composition of
1566 peridotites and their minerals: a laser-ablation ICPMS study. *Earth and*
1567 *Planetary Science Letters*, 154(1-4):53–71.

1568 Engler, O. and Randle, V. (2009). *Introduction to Texture Analysis: Macrotexture,*
1569 *Microtexture, and Orientation Mapping*.

1570 Fang, X., Yin, W., Qin, C., Wang, W., Lo, K., and Shek, C. (2016). The
1571 interface character distribution of cold-rolled and annealed duplex stainless steel.
1572 *Materials Characterization*, 118:397–404.

1573 Farla, R. J. M., Peach, C. J., and ten Grotenhuis, S. M. (2010). Electrical
1574 conductivity of synthetic iron-bearing olivine. *Physics and Chemistry of*
1575 *Minerals*, 37(3):167–178.

1576 Farver, J. R. and Yund, A. (2000). Silicon diffusion in forsterite aggregates:
1577 Implications for diffusion accommodated creep. *Geophysical research letters*,
1578 27(15):2337–2340.

1579 Farver, J. R., Yund, R. A., and Rubie, D. C. (1994). Magnesium grain boundary
1580 diffusion in forsterite aggregates at 1000-1300C and 0.1 MPa to 10 GPa. *Journal*
1581 *of Geophysical Research: Solid Earth*, 99(B10):19809–19819.

1582 Faul, U. and Jackson, I. (2015). Transient Creep and Strain Energy Dissipation:
1583 An Experimental Perspective. *Annual Review of Earth and Planetary Sciences*,
1584 43(1):541–569.

1585 Faul, U. H. (2000). Chapter 3 Constraints on the Melt Distribution in Anisotropic
1586 Polycrystalline Aggregates Undergoing Grain Growth. In Bagdassarov, N.,
1587 Laporte, D., and Thompson, A., editors, *Physics and Chemistry of Partially*
1588 *Molten Rocks*, volume Chapter 3, chapter 3, pages 67–92. Kluwer Academic
1589 Publishers, Dordrecht, 2000.

1590 Faul, U. H., Cline, C. J., David, E. C., Berry, A. J., and Jackson, I. (2016).
1591 Titanium-hydroxyl defect-controlled rheology of the Earth's upper mantle.
1592 *Earth and Planetary Science Letters*, 452:227–237.

1593 Faul, U. H. and Fitz Gerald, J. D. (1999). Grain misorientations in partially
1594 molten olivine aggregates: an electron backscatter diffraction study. *Physics*
1595 *and Chemistry of Minerals*, 26(3):187–197.

1596 Faul, U. H., Fitz Gerald, J. D., and Jackson, I. (2004). Shear wave attenuation
1597 and dispersion in melt-bearing olivine polycrystals: 2. Microstructural
1598 interpretation and seismological implications. *Journal of Geophysical Research*,
1599 109(B6):B06202.

1600 Faul, U. H. and Jackson, I. (2007). Diffusion creep of dry, melt-free olivine. *Journal*
1601 *of Geophysical Research*, 112(B4):B04204.

1602 Faul, U. H. and Scott, D. (2006). Grain growth in partially molten olivine
1603 aggregates. *Contributions to Mineralogy and Petrology*, 151(1):101–111.

1604 Faul, U. H., Toomey, D. R., and Waff, H. S. (1994). Intergranular balsaltic melt is
1605 dristibuted in thin, eleogated inclusions. *Geophysical Research Letters*, 21(1):29–
1606 32.

1607 Fei, H., Koizumi, S., Sakamoto, N., Hashiguchi, M., Yurimoto, H., Marquardt, K.,
1608 Miyajima, N., Yamazaki, D., and Katsura, T. (2016). New constraints on upper
1609 mantle creep mechanism inferred from silicon grain-boundary diffusion rates.
1610 *Earth and Planetary Science Letters*, 433(433):350–359.

1611 Fliervoet, T. F., Drury, M. R., and Chopra, P. N. (1999). Crystallographic
1612 preferred orientations and misorientations in some olivine rocks deformed by
1613 diffusion or dislocation creep. *Tectonophysics*, 303(1-4):1–27.

1614 Foley, S. F., Jacob, D. E., and O'Neill, H. S. C. (2011). Trace element variations
1615 in olivine phenocrysts from Ugandan potassic rocks as clues to the chemical
1616 characteristics of parental magmas. *Contributions to Mineralogy and Petrology*,
1617 162(1):1–20.

1618 Foley, S. F., Prelevic, D., Rehfeldt, T., and Jacob, D. E. (2013). Minor and trace
1619 elements in olivines as probes into early igneous and mantle melting processes.
1620 *Earth and Planetary Science Letters*, 363:181–191.

1621 Garapic, G., Faul, U. H., and Brisson, E. (2013). High-resolution imaging of the
1622 melt distribution in partially molten upper mantle rocks: evidence for wetted
1623 two- grain boundaries. *Geochemistry, Geophysics, Geosystems*, 14(Xx):1–11.

1624 Gardés, E., Wunder, B., Marquardt, K., and Heinrich, W. (2012). The effect of
1625 water on intergranular mass transport: new insights from diffusion-controlled
1626 reaction rims in the MgOSiO2 system. *Contributions to Mineralogy and*
1627 *Petrology*, 164(1):1–16.

1628 Garrido, C. J., Bodinier, J.-L., and Alard, O. (2000). Incompatible trace element
1629 partitioning and residence in anhydrous spinel peridotites and websterites from
1630 the Ronda orogenic peridotite. *Earth and Planetary Science Letters*, 181(3):341–
1631 358.

Ghanbarzadeh, S., Prodanović, M., and Hesse, M. a. (2014). Percolation and Grain Boundary Wetting in Anisotropic Texturally Equilibrated Pore Networks. *Physical Review Letters*, 113(4):048001.

Ghosh, D. B. and Karki, B. B. (2014). First principles simulations of the stability and structure of grain boundaries in Mg2SiO4 forsterite. *Physics and Chemistry of Minerals*, 41:163–171.

Goetze, C., Kohlstedt, D. L., and Sciences, P. (1973). Laboratory Study of Dislocation Climb and Diffusion in Olivine. *Journal of Geophysical Research*, 78(26).

Gribb, T. T. and Cooper, R. F. (1998). Low-frequency shear attenuation in polycrystalline olivine: Grain boundary diffusion and the physical significance of the Andrade model for viscoelastic rheology. *Journal of Geophysical Research: Solid Earth*, 103(B11):27267–27279.

Gurmani, S. F., Jahn, S., Brasse, H., and Schilling, F. R. (2011). Atomic scale view on partially molten rocks: Molecular dynamics simulations of melt-wetted olivine grain boundaries. *Journal of Geophysical Research*, 116(B12):B12209.

Han, L.-b., An, Q., Fu, R.-s., Zheng, L., and Luo, S.-n. (2010). Local and bulk melting of Cu at grain boundaries. *Physical Review B*, 405:748–753.

Hansen, L., Zimmerman, M., Dillman, A., and Kohlstedt, D. (2012a). Strain localization in olivine aggregates at high temperature: A laboratory comparison of constant-strain-rate and constant-stress boundary conditions. *Earth and Planetary Science Letters*, 333-334:134–145.

Hansen, L., Zimmerman, M., and Kohlstedt, D. (2012b). Laboratory measurements of the viscous anisotropy of olivine aggregates. *Nature*, 492(7429):415–418.

Hansen, L. N., Zimmerman, M. E., and Kohlstedt, D. L. (2011). Grain boundary sliding in San Carlos olivine: Flow law parameters and crystallographic-preferred orientation. *Journal of Geophysical Research*, 116(B8):B08201.

Hansen, L. N., Zimmerman, M. E., and Kohlstedt, D. L. (2012c). The influence of microstructure on deformation of olivine in the grain-boundary sliding regime. *Journal of Geophysical Research: Solid Earth*, 117(B9):n/a–n/a.

Harmer, M. P. (2010). Interfacial Kinetic Engineering: How Far Have We Come Since Kingery's Inaugural Sosman Address? *Journal of the American Ceramic Society*, 93(2):301–317.

Hartmann, K., Wirth, R., and Heinrich, W. (2010). Synthetic near $\Sigma 5$ (210)/[100] grain boundary in YAG fabricated by direct bonding: structure and stability. *Physics and Chemistry of Minerals*, 37(5):291–300.

Hartmann, K., Wirth, R., and Markl, G. (2008). P-T-X-controlled element transport through granulite-facies ternary feldspar from Lofoten, Norway. *Contributions to Mineralogy and Petrology*, 156(3):359–375.

Hashim, L. (2016). *Unraveling the grain size evolution in the Earth ' s mantle Experimental observations and theoretical modeling*. PhD thesis.

Hayden, L. A. and Watson, E. B. (2008). Grain boundary mobility of carbon in Earth's mantle: a possible carbon flux from the core. *Proceedings of the National Academy of Sciences of the United States of America*, 105(25):8537–41.

Heilbronner, R. and Tullis, J. (2006). Evolution of c axis pole figures and grain size during dynamic recrystallization: Results from experimentally sheared quartzite. *Journal of Geophysical Research: Solid Earth*, 111:1–19.

Heinemann, S., Wirth, R., and Dresen, G. (2001). Synthesis of feldspar bicrystals by direct bonding. *Physics and Chemistry of Minerals*, 28(10):685–692.

Heinemann, S., Wirth, R., Dresen, G., and Paper, O. (2003). TEM study of a special grain boundary in a synthetic K-feldspar bicrystal: Manebach twin. *Physics and Chemistry of Minerals*, 30(3):125–130.

Heinemann, S., Wirth, R., Gottschalk, M., and Dresen, G. (2005). Synthetic [100] tilt grain boundaries in forsterite: 9.9 to 21.5. *Physics and Chemistry of Minerals*, 32(4):229–240.

Hiraga, T., Anderson, I., Zimmerman, M., Mei, S., and Kohlstedt, D. (2002). Structure and chemistry of grain boundaries in deformed, olivine + basalt and partially molten lherzolite aggregates: evidence of melt-free grain boundaries. *Contributions to Mineralogy and Petrology*, 144:163–175.

Hiraga, T., Anderson, I. M., and Kohlstedt, D. L. (2004). Grain boundaries as reservoirs of incompatible elements in the Earth's mantle. *Nature*, 427(6976):699–703.

Hiraga, T., Anderson, I. M., Kohlstedt, D. L., Iraga, T. A. H., Nderson, I. A. N. M. A., and Ohlstedt, D. A. L. K. (2003). Chemistry of grain boundaries in mantle rocks. *American Mineralogist*, 88(6976):1015–1019.

Hiraga, T., Hirschmann, M. M., and Kohlstedt, D. L. (2007). Equilibrium interface segregation in the diopside-forsterite system II: Applications of interface enrichment to mantle geochemistry. *Geochimica et Cosmochimica Acta*, 71(5):1281–1289.

Hiraga, T. and Kohlstedt, D. L. (2007). Equilibrium interface segregation in the diopside-forsterite system I: Analytical techniques, thermodynamics, and segregation characteristics. *Geochimica et Cosmochimica Acta*, 71(5):1266–1280.

Hiraga, T., Tachibana, C., Ohashi, N., and Sano, S. (2010). Grain growth systematics for forsterite enstatite aggregates: Effect of lithology on grain size in the upper mantle. *Earth and Planetary Science Letters*, 291(1-4):10–20.

Hirth, G. and Kohlstedt, D. (2003). Rheology of the Upper mantle and the mantle Wedge: a View from the Experimentalists. In *Inside the Subduction Factory*, chapter Greg Hirth, page 311.

Hirth, G. and Kohlstedt, D. L. (1995). Experimental constraints on the dynamics of the partially molten upper mantle: Deformation in the diffusion creep regime. *Journal of Geophysical Research*, 100(B2):1981–2001.

Holm, E. A., Rohrer, G. S., Foiles, S. M., Rollett, A. D., Miller, H. M., and Olmsted, D. L. (2011). Validating computed grain boundary energies in fcc metals using the grain boundary character distribution. *Acta Materialia*, 59(13):5250–5256.

1717 Homer, E. R., Patala, S., and Priedeman, J. L. (2015). Grain Boundary
1718 Plane Orientation Fundamental Zones and Structure-Property Relationships.
1719 *Scientific Reports*, 5:15476.

1720 Jackson, I., Faul, U. H., Fitz Gerald, J. D., and Tan, B. H. (2004). Shear
1721 wave attenuation and dispersion in melt-bearing olivine polycrystals: 1.
1722 Specimen fabrication and mechanical testing. *Journal of Geophysical Research*,
1723 109(B6):B06201.

1724 Jackson, I., Fitz Gerald, J. D., Faul, U. H., and Tan, B. H. (2002). Grain-
1725 size-sensitive seismic wave attenuation in polycrystalline olivine. *Journal of*
1726 *Geophysical Research: Solid Earth*, 107(B12):ECV 5–1–ECV 5–16.

1727 Johnson, C. L., Hÿtch, M. J., Buseck, P. R., and Hy, M. J. (2004). Nanoscale
1728 waviness of low-angle grain boundaries. *Proceedings of the National Academy*
1729 *of Sciences of the United States of America*, 101(52):17936–17939.

1730 Jurewicz, S. R. and Jurewicz, A. J. G. (1986). Distribution of apparent angles
1731 on random sections with emphasis on dihedral angle measurements. *Journal of*
1732 *Geophysical Research*, 91(B9):9277.

1733 Kahneman, D. and Tversky, A. (1981). On the Study of Statistical Intuitions.
1734 *ONR technical report*.

1735 Kaplan, W. D., Chatain, D., Wynblatt, P., and Carter, W. C. (2013). A review
1736 of wetting versus adsorption, complexions, and related phenomena: The rosetta
1737 stone of wetting. *Journal of Materials Science*, 48(17):5681–5717.

1738 Karato, S. (1989). Grain growth kinetics in olivine aggregates. *Tectonophysics*,
1739 168(4):255–273.

1740 Karato, S.-I., Paterson, M. S., and FitzGerald, J. D. (1986). Rheology of synthetic
1741 olivine aggregates: Influence of grain size and water. *Journal of Geophysical*
1742 *Research*, 91(B8):8151.

1743 Karato, S.-i., Toriumi, M., and Fujii, T. (1980). Dynamic recrystallization of olivine
1744 single crystals during high-temperature creep. *Geophysical Research Letters*,
1745 7(9):649–652.

1746 Kaur, I., Mishin, Y., and Gust, W. (1995). *Fundamentals of grain and interphase*
1747 *boundary diffusion*. Wiley & Sons, Chichester, 3 edition.

1748 Kelly, M. N., Bojarski, S. A., and Rohrer, G. S. (2016). The Temperature
1749 Dependence of the Relative Grain-Boundary Energy of Yttria-doped Alumina.
1750 *J. American Ceramic Society*, 7:1–7.

1751 Kim, C.-S., Rollett, A. D., and Rohrer, G. S. (2006). Grain boundary planes: New
1752 dimensions in the grain boundary character distribution. *Scripta Materialia*,
1753 54(6):1005–1009.

1754 King, H. E., Plümper, O., Geisler, T., and Putnis, A. (2011). Experimental
1755 investigations into the silicification of olivine: Implications for the reaction
1756 mechanism and acid neutralization. *American Mineralogist*, 96(10):1503–1511.

1757 King, H. E., Stimpfl, M., Deymier, P., Drake, M. J., Catlow, C. R. A., Putnis, A.,
1758 and de Leeuw, N. H. (2010). Computer simulations of water interactions with
1759 low-coordinated forsterite surface sites: Implications for the origin of water in
1760 the inner solar system. *Earth and Planetary Science Letters*, 300(1-2):11–18.

1761 Kingery, W. D. (1974). Plausible Concepts Necessary and Sufficient for
1762 Interpretation of Ceramic Grain-Boundary Phenomena: I, Grain -Boundary
1763 characteristics, Structure, and Electrostatic Potential. *Journal of the American*
1764 *Ceramic Society*, 57(1):1–8.

1765 Kiss, Á. K., Rauch, E. F., and Lábár, J. L. (2016). Highlighting material
1766 structure with transmission electron diffraction correlation coefficient maps.
1767 *Ultramicroscopy*, 163:31–37.

1768 Kleebe, H.-J. (2002). Comparison between SEM and TEM Imaging
1769 Techniques to Determine Grain-Boundary Wetting in Ceramic Polycrystals.
1770 *Journal of the American Ceramic Society*, 85(1 %R doi:10.1111/j.1151-
1771 2916.2002.tb00036.x):43–48.

1772 Kliewer, K. L. and Koehler, J. S. (1965). Space charge in ionic crystals I. General
1773 approach with applictaion to NaCl. *Physical Review*, 140(4A).

1774 Koch, C. T., Bhattacharyya, S., Rühle, M., Satet, R. L., and Hoffmann,
1775 M. J. (2006). Measuring Electrostatic Potential Profiles across Amorphous
1776 Intergranular Films by Electron Diffraction. *Microscopy and Microanalysis*,
1777 12(02):160–169.

1778 Kohlstedt, D. L. (1990). Chemical analysis of grain boundaries in an olivine-basalt
1779 aggregate using high-resolution, analytical electron microscopy. In *The Brittle-*
1780 *Ductile Transition in Rocks*, pages 211–218. American Geophysical Union.

1781 Kohlstedt, D. L. and Hansen, L. N. (2015). *Properties of Rocks and Minerals -*
1782 *Constitutive Equations, Rheological Behavior, and Viscosity of Rocks*, volume 2.
1783 Elsevier B.V.

1784 Koizumi, S., Hiraga, T., Tachibana, C., Tasaka, M., Miyazaki, T., Kobayashi, T.,
1785 Takamasa, A., Ohashi, N., and Sano, S. (2010). Synthesis of highly dense and
1786 fine-grained aggregates of mantle composites by vacuum sintering of nano-sized
1787 mineral powders. *Physics and Chemistry of Minerals*, 37(8):505–518.

1788 Langdon, T. G. (2006). Grain boundary sliding revisited: Developments in sliding
1789 over four decades. *Journal of Materials Science*, 41(3):597–609.

1790 Laporte, D. and Provost, A. (2000). Equilibrium geometry of a fluid phase
1791 in a polycrystalline aggregate with anisotropic surface energies: Dry grain
1792 boundaries. *Journal of Geophysical Research: Solid Earth*, 105(B11):25937–
1793 25953.

1794 Laumonier, M., Farla, R., Frost, D. J., Katsura, T., Marquardt, K., Bouvier,
1795 A.-s., and Baumgartner, L. P. (2017). Experimental determination of melt
1796 interconnectivity and electrical conductivity in the upper mantle. *Earth and*
1797 *Planetary Science Letters*, 463:286–297.

1798 Lee, C.-T. A., Harbert, A., and Leeman, W. P. (2007). Extension of lattice
1799 strain theory to mineral/mineral rare-earth element partitioning: An approach
1800 for assessing disequilibrium and developing internally consistent partition
1801 coefficients between olivine, orthopyroxene, clinopyroxene and basaltic melt.
1802 *Geochimica et Cosmochimica Acta*, 71(2):481–496.

1803 Lehovec, K. (1953). Space-Charge Layer and distribution of lattice defects at the
1804 surface of ionic crystals. *The Journal of Chemical Physics*, 21(May 2010):1123–
1805 1128.

1806 Lejcek, P. (2010). Grain Boundaries : Description , Structure and
1807 Thermodynamics. In *Grain boundary Segregation in Metals*, page 239.

1808 Levine, J. S., Mosher, S., and Rahl, J. M. (2016). The role of subgrain boundaries
1809 in partial melting. *Journal of Structural Geology*, 89:181–196.

1810 Lloyd, G. E., Farmer, A. B., and Mainprice, D. (1997). Misorientation analysis and
1811 the formation and orientation of subgrain and grain boundaries. *Tectonophysics*,
1812 279(1-4):55–78.

1813 Luo, J. (2012). Developing interfacial phase diagrams for applications in activated
1814 sintering and beyond: Current status and future directions. *Journal of the*
1815 *American Ceramic Society*, 95(8):2358–2371.

1816 Luo, J. and Chiang, Y.-M. (2008). Wetting and Prewetting on Ceramic Surfaces.
1817 *Annual Review of Materials Research*, 38(1):227–249.

1818 Luo, J., Gupta, V. K., Yoon, D. H., and Meyer, H. M. (2005). Segregation-induced
1819 grain boundary premelting in nickel-doped tungsten. *Applied Physics Letters*,
1820 87(23):1–3.

1821 Mackenzie, J. K. (1958). Second Paper on Statistics Associated with the Random
1822 Disorientation of Cubes. *Biometrika*, 45(1/2):229.

1823 Maher, K., Johnson, N. C., Jackson, A., Lammers, L. N., Torchinsky, A. B.,
1824 Weaver, K. L., Bird, D. K., and Brown, G. E. (2016). A spatially resolved
1825 surface kinetic model for forsterite dissolution. *Geochimica et Cosmochimica*
1826 *Acta*, 174:313–334.

1827 Maitland, T. and Sitzman, S. (2007). Electron Backscatter Diffraction (EBSD)
1828 Technique and Materials Characterization Examples. In *Scanning Microscopy*
1829 *for Nanotechnology*, chapter Scanning M, pages 41–75.

1830 Mantisi, B., Sator, N., and Guillot, B. (2017). Structure and transport at grain
1831 boundaries in polycrystalline olivine: An atomic-scale perspective. *Geochimica*

et Cosmochimica Acta, 219:160–176.

Marquardt, H., Gleason, a., Marquardt, K., Speziale, S., Miyagi, L., Neusser, G., Wenk, H.-R., and Jeanloz, R. (2011a). Elastic properties of MgO nanocrystals and grain boundaries at high pressures by Brillouin scattering. *Physical Review B*, 84(6):064131.

Marquardt, H., Speziale, S., Marquardt, K., Reichmann, H. J., Konôpková, Z., Morgenroth, W., and Liermann, H. P. (2011b). The effect of crystallite size and stress condition on the equation of state of nanocrystalline MgO. *Journal of Applied Physics*, 110(11):8–12.

Marquardt, K., Petrishcheva, E., Gardés, E., Wirth, R., Abart, R., Heinrich, W., and Garde, E. (2011c). Grain boundary and volume diffusion experiments in yttrium aluminium garnet bicrystals at 1,723 K: a miniaturized study. *Contributions to Mineralogy and Petrology*, 162(4):739–749.

Marquardt, K., Ramasse, Q. M., Kisielowski, C., Wirth, R., M, K., R, Q. M., and K, C. (2011d). Diffusion in yttrium aluminium garnet at the nanometer-scale: Insight into the effective grain boundary width. *American Mineralogist*, 96(10):1521–1529.

Marquardt, K., Rohrer, G. S., Morales, L., Rybacki, E., Marquardt, H., and Lin, B. (2015). The most frequent interfaces in olivine aggregates: the GBCD and its importance for grain boundary related processes. *Contributions to Mineralogy and Petrology*, 170(4):40.

Maruyama, G. and Hiraga, T. (2017a). Grain- to multiple-grain-scale deformation processes during diffusion creep of forsterite + diopside aggregate: 2. Grain boundary sliding-induced grain rotation and its role in crystallographic preferred orientation in rocks. *Journal of Geophysical Research: Solid Earth*.

Maruyama, G. and Hiraga, T. (2017b). Grain- to multiple-grain-scale deformation processes during diffusion creep of forsterite + diopside aggregate I: Direct observations. *Journal of Geophysical Research: Solid Earth*.

McClay, K. R. (1977). Pressure solution and Coble creep in rocks and minerals: a review. *Journal of the Geological Society*, 134(1):57–70.

Mcdonnell, R. D. and Spiers, C. J. (2002). Fabrication of dense forsterite enstatite polycrystals for experimental studies. *Physics and Chemistry of Minerals*, 29:19–31.

Mei, Q. S. and Lu, K. (2007). Melting and superheating of crystalline solids : From bulk to nanocrystals. *Progress in Materials Science*, 52:1175–1262.

Mei, S. and Kohlstedt, D. L. (2000). Influence of water on plastic deformation of olivine aggregates 2. Dislocation creep regime. *J. Geophys. Res.*, 105(B9):21471–21481.

Mellenthin, J., Karma, A., and Plapp, M. (2008). Phase-field crystal study of grain-boundary premelting. *Physical Review B*, 78(18):184110.

Milas, I., Hinnemann, B., and Carter, E. A. (2008). Structure of and ion segregation to an alumina grain boundary: Implications for growth and creep. *Journal of Materials Research*, 23(5):1494–1508.

Miletich, R., Nowak, M., Seifert, F., Angel, R. J., and Brandstätter, G. (1999). High-pressure crystal chemistry of chromous orthosilicate, Cr 2 SiO 4 . A single-crystal X-ray diffraction and electronic absorption spectroscopy study. *Structure*, 26:446–459.

Milke, R., Dohmen, R., Becker, H.-W., and Wirth, R. (2007). Growth kinetics of enstatite reaction rims studied on nano-scale, Part I: Methodology, microscopic observations and the role of water. *Contributions to Mineralogy and Petrology*, 154(5):519–533.

Milke, R., Wiedenbeck, M., and Heinrich, W. (2001). Grain boundary diffusion of Si, Mg, and O in enstatite reaction rims; a SIMS study using isotopically doped reactants. *Contributions to Mineralogy and Petrology*, 142(1):15–26.

Mishin, Y. and Herzig, C. (1999). Grain boundary diffusion: recent progress and future research. *Materials Science and Engineering: A*, 260(1-2):55–71.

Mistler, R. E. and Coble, R. L. (1974). Grain-boundary diffusion and boundary widths in metals and ceramics. *Journal of Applied Physics*, 45(4):1507.

Miyazaki, T., Sueyoshi, K., and Hiraga, T. (2013). Olivine crystals align during diffusion creep of Earth's upper mantle. *Nature*, 502(7471):321–326.

Morris, S. J. S. and Jackson, I. (2009). Diffusionally assisted grain-boundary sliding and viscoelasticity of polycrystals. *Journal of the Mechanics and Physics of Solids*, 57(4):744–761.

Morrow, C. P., Kubicki, J. D., Mueller, K. T., and Cole, D. R. (2010). Description of Mg 2 + Release from Forsterite Using Ab Initio Methods . pages 5417–5428.

Mott, N. (1951). The mechanical properties of metals. *Proceedings of the physical society*, 64(9):416.

Mu, S. and Faul, U. H. (2016). Grain boundary wetness of partially molten dunite. *Contributions to Mineralogy and Petrology*, 171(5):1–15.

Mussi, A., Cordier, P., Demouchy, S., and Vanmansart, C. (2014). Characterization of the glide planes of the [001] screw dislocations in olivine using electron tomography. *Physics and Chemistry of Minerals*, 41(7):537–545.

Nakamura, A. and Schmalzried, H. (1983). On the nonstoichiometry and point defects of olivine. *Physics and Chemistry of Minerals*, 10(1):27–37.

Nichols, S. J. and Mackwell, S. J. (1991). Grain growth in porous olivine aggregates. *Physics and Chemistry of Minerals*, 18(4):269–278.

Ohuchi, T. and Nakamura, M. (2007). Grain growth in the forsteritediopside system. *Physics of the Earth and Planetary Interiors*, 160(1):1–21.

Ohuchi, T., Nakamura, M., and Michibayashi, K. (2010). Effect of grain growth on cation exchange between dunite and fluid: Implications for chemical homogenization in the upper mantle. *Contributions to Mineralogy and Petrology*, 160(3):339–357.

Oleg, P. and Jacques, S. (2007). Kinetics and mechanism of natural fluorapatite dissolution at 25C and pH from 3 to 12. *Geochimica et Cosmochimica Acta*, 71(24):5901–5912.

1917 Olmsted, D. L., Foiles, S. M., and Holm, E. a. (2009). Survey of computed grain
1918 boundary properties in face-centered cubic metals: I. Grain boundary energy.
1919 *Acta Materialia*, 57(13):3694–3703.

1920 Palmero, P., Fantozzi, G., Lomello, F., Bonnefont, G., and Montanaro, L. (2012).
1921 Creep behaviour of alumina / YAG composites prepared by different sintering
1922 routes. *Ceramics International*, 38(1):433–441.

1923 Pang, Y. and Wynblatt, P. (2006). Effects of Nb Doping and Segregation on the
1924 Grain Boundary Plane Distribution in TiO2. *Journal of the American Ceramic*
1925 *Society*, 89(2):666–671.

1926 Parman, S. W., Kurz, M. D., Hart, S. R., and Grove, T. L. (2005). Helium solubility
1927 in olivine and implications for high 3He/4He in ocean island basalts. *Nature*,
1928 437(7062):1140–1143.

1929 Paterson, M. S. (1990). Rock deformation experimentation. volume 56, pages
1930 187–194.

1931 Peterson, N. L. (1983). Grain-boundary diffusion in metals. *International Metals*
1932 *Reviews*, 28(2).

1933 Petry, C., Chakraborty, S., Palme, H., Etry, C. H. P., Hakraborty, S. U. C., and
1934 Alme, H. E. P. (2004). Experimental determination of Ni diffusion coefficients in
1935 olivine and their dependence on temperature, composition, oxygen fugacity, and
1936 crystallographic orientation. *Geochimica et Cosmochimica Acta*, 68(20):4179–
1937 4188.

1938 Phakey, P., Dollinger, G., and Christie, J. (1972). Transmission electron
1939 microscopy of experimentally deformed olivine crystals. *American Mineralogist*,
1940 61:117–138.

1941 Poirier, J.-P. (1985). *Creep of crystals : high-temperature deformation processes in*
1942 *metals, ceramics, and minerals*. Cambridge University Press.

1943 Raabe, D., Herbig, M., Sandlöbes, S., Li, Y., Tytko, D., Kuzmina, M., Ponge,
1944 D., and Choi, P. P. (2014). Grain boundary segregation engineering in metallic
1945 alloys: A pathway to the design of interfaces. *Current Opinion in Solid State*

and Materials Science, 18(4):253–261.

Raj, R. and Ashby, M. F. (1971). On Grain Boundary Sliding and Diffusional Creep. *Metallurgical Transactions*, 2(April):113–1127.

Randle, V. and Davies, H. (2002). A comparison between three-dimensional and two-dimensional grain boundary plane analysis. *Ultramicroscopy*, 90(2-3):153–162.

Rasmussen, D. R., Simpson, Y. K., Kilaas, R., and Carter, C. B. (1989). Contrast effects at grooved interfaces. *Ultramicroscopy*, 30:52–57.

Raterron, P., Bussod, G. Y., Doukhan, N., and Doukhan, J.-C. (1997). Early partial melting in the upper mantle: an A.E.M. study of a lherzolite experimentally annealed at hypersolidus conditions. *Tectonophysics*, 279(1-4):79–91.

Raterron, P., Chopra, P., and Doukhan, J. C. (2000). SiO2 precipitation in olivine: ATEM investigation of two dunites annealed at 300 MPa in hydrous conditions. *Earth and Planetary Science Letters*, 180(3-4):415–423.

Raterron, P., Ingrin, J., Jaoul, O., Doukhan, N., and Elie, F. (1995). Early Partial Melting of Diopside Under High-Pressure. *Physics of the Earth and Planetary Interiors*, 89(1-2):77–88.

Read, W. T. and Schockley, W. (1950). Dislocation models of crystal grain boundaries. *Physical Review*, 78(3).

Reed, B., Adams, B., Bernier, J., Hefferan, C., Henrie, A., Li, S., Lind, J., Suter, R., and Kumar, M. (2012). Experimental tests of stereological estimates of grain boundary populations. *Acta Materialia*, 60(6-7):2999–3010.

Ricoult, D. L. and Kohlstedt, D. L. (1983). Structural width of low-angle grain boundaries in olivine. *Physics and Chemistry of Minerals*, 9(3-4):133–138.

Roberts, J. J. and Tyburczy, J. A. (1991). Frequency dependent electrical properties of polycrystalline olivine compacts. *Journal of Geophysical Research*, 96(B10):16205.

1974 Rohrer, G. S. (2007). The distribution of grain boundary planes in polycrystals.
1975 *JOM: The Journal of The Minerals, Metals & Materials Society (TMS)*,
1976 59(9):38–42.

1977 Rohrer, G. S. (2011a). Grain boundary energy anisotropy: a review. *Journal of*
1978 *Materials Science*, 46(18):5881–5895.

1979 Rohrer, G. S. (2011b). Measuring and Interpreting the Structure of Grain-
1980 Boundary Networks. *Journal of the American Ceramic Society*, 94(3):633–646.

1981 Rohrer, G. S. (2015). The role of grain boundary energy in grain boundary
1982 complexion transitions. *Current Opinion in Solid State and Materials Science*,
1983 20(5):231–239.

1984 Rohrer, G. S., Saylor, D. M., El Dasher, B., Adams, B. L., Rollett, A. D., and
1985 Wynblatt, P. (2004). The distribution of internal interfaces in polycrystals.
1986 *Zeitschrift für Metallkunde*, 95(4):197–214.

1987 Rollett, A. and Rohrer, G. S. (2017). *Recrystallization and Related Annealing*
1988 *Phenomena*.

1989 Rollett, A. D. (2004). Crystallographic texture Change during Grain Growth.
1990 *Jom*, 56(4):63–68.

1991 Rollett, A. D., Gottstein, G., Shvindlerman, L. S., and Molodov, D. a. (2004).
1992 Grain boundary mobility a brief review. *Zeitschrift für Metallkunde*, 95(4):226–
1993 229.

1994 Romeu, D. (2003). Interfaces and quasicrystals as competing crystal lattices :
1995 Towards a crystallographic theory of interfaces. pages 1–12.

1996 Sader, K., Brown, A., Brydson, R., and Bleloch, A. (2010). Quantitative analysis of
1997 image contrast in phase contrast STEM for low dose imaging. *Ultramicroscopy*,
1998 110(10):1324–1331.

1999 Sano, S., Saito, N., Matsuda, S.-i., Ohashi, N., and Haneda, H. (2006). Synthesis of
2000 High Density and Transparent Forsterite Ceramics Using Nano-Sized Precursors
2001 and Their Dielectric Properties. *Journal of the American Ceramic Society*,
2002 574(89):568–574.

2003 Sano, T., Kim, C. S., and Rohrer, G. S. (2005). Shape evolution of SrTiO 3
2004 crystals during coarsening in a titania-rich liquid. *Journal of the American*
2005 *Ceramic Society*, 88(4):993–996.

2006 Sano, T., Saylor, D. M., and Rohrer, G. S. (2003). Surface Energy Anisotropy
2007 of SrTiO 3 at 1400 C in Air. *Journal of the American Ceramic Society*,
2008 86(11):1933–1939.

2009 Saylor, D. M. (2001). The Character Dependence of Interfacial Energies in
2010 Magnesia. pages 1–178.

2011 Saylor, D. M., El Dasher, B. S., Rollett, A. D., and Rohrer, G. S. (2004).
2012 Distribution of grain boundaries in aluminum as a function of five macroscopic
2013 parameters. *Acta Materialia*, 52(12):3649–3655.

2014 Saylor, D. M., Morawiec, A., and Rohrer, G. S. (2003). Distribution of grain
2015 boundaries in magnesia as a function of five macroscopic parameters. *Acta*
2016 *Materialia*, 51(13):3675–3686.

2017 Schäfer, F. N. and Foley, S. F. (2002). The effect of crystal orientation on the
2018 wetting behaviour of silicate melts on the surfaces of spinel peridotite minerals.
2019 *Contributions to Mineralogy and Petrology*, 143(2):254–261.

2020 Seifert, S. and O'Neill, H. S. C. (1986). Experimental determination of activity-
2021 composition relations in Ni2SiO4-Mg2Sio4 and Co2SiO4-Mg2Sio4 olivine sloid
2022 solutions at 1200K. *Geochemica et Cosmochemica Acta*, 51:97–104.

2023 Shirpour, M., Merkle, R., Lin, C. T., and Maier, J. (2012). Nonlinear electrical
2024 grain boundary properties in proton conducting YBaZrO3 supporting the space
2025 charge depletion model. *Physical Chemistry Chemical Physics*, 14(2):730.

2026 Smith, C. S. (1948). Introduction to Grains, Phases, and Interfaces-an
2027 Interpretation of Microstructure. *Trans. Met. Soc. AIME*, 175:15–51.

2028 Solomon, S. C. (1972). Seismic-Wave and Partial Melting in the Upper Mantle of
2029 North America. *Journal of Geophysical Research*, 77(8).

2030 Sommer, H., Regenauer-Lieb, K., Gasharova, B., and Siret, D. (2008). Grain
2031 boundaries: a possible water reservoir in the Earth's mantle? *Mineralogy and*

Petrology, 94(1-2):1–8.

Steinbach, I. (2009). Phase-field models in materials science. *Modelling and Simulation in Materials Science and Engineering*, 17(7):073001.

Sun, X.-Y., Cordier, P., Taupin, V., Fressengeas, C., and Jahn, S. (2016). Continuous description of a grain boundary in forsterite from atomic scale simulations: the role of disclinations. *Philosophical Magazine*, 96(17):1757–1772.

Sundberg, M. and Cooper, R. F. (2008). Crystallographic preferred orientation produced by diffusional creep of harzburgite: Effects of chemical interactions among phases during plastic flow. *Journal of Geophysical Research: Solid Earth*, 113(12):1–16.

Sutton, A. P. and Balluffi, R. W. (1995). *Interfaces in crystalline materials*, volume 51. Clarendon Press.

Takei, Y. (1998). Constitutive mechanical relations of solid-liquid composites in terms of grain boundary contiguity. *Journal of Geophysical Research*, 103(98):18183–18203.

Takei, Y. (2017). Effects of Partial Melting on Seismic Velocity and Attenuation: A New Insight From Experiments. *Ann. Rev. Earth Planet. Sci.*, pages 1–25.

Takei, Y. and Holtzman, B. K. (2009a). Viscous constitutive relations of solid-liquid composites in terms of grain boundary contiguity : 2 . Compositional model for small melt fractions. 114:1–18.

Takei, Y. and Holtzman, B. K. (2009b). Viscous constitutive relations of solid-liquid composites in terms of grain boundary contiguity: 1. Grain boundary diffusion control model. *Journal of Geophysical Research: Solid Earth*, 114(6):1–19.

Tan, B. H., Jackson, I., and Fitz Gerald, J. D. (1997). Shear wave dispersion and attenuation in fine-grained synthetic olivine aggregates: Preliminary results. *Geophysical Research Letters*, 24(9):1055–1058.

Tan, B. H., Jackson, I., and Fitz Gerald, J. D. (2001). High-temperature viscoelasticity of fine-grained polycrystalline olivine. *Physics and Chemistry*

of Minerals, 28(9):641–664.

Tasaka, M., Hiraga, T., and Zimmerman, M. E. (2013). Influence of mineral fraction on the rheological properties of forsterite+enstatite during grain-size-sensitive creep: 2. Deformation experiments. *Journal of Geophysical Research: Solid Earth*, 118(8):3991–4012.

ten Grotenhuis, S. M., Drury, M. R., Peach, C. J., and Spiers, C. J. (2004). Electrical properties of fine-grained olivine: Evidence for grain boundary transport. *Journal of Geophysical Research B: Solid Earth*, 109(6):1–9.

ten Grotenhuis, S. M., Drury, M. R., Spiers, C. J., and Peach, C. J. (2005). Melt distribution in olivine rocks based on electrical conductivity measurements. *Journal of Geophysical Research*, 110(B12):B12201.

Toramaru, A. and Fujii, N. (1986a). Connectivity of melt phase in a partially molten peridotite. *Journal of Geophysical Research*, 91(B9):9239.

Toramaru, A. and Fujii, N. (1986b). Connectivity of melt phase in a partially molten upper mantle rocks from experiments and percolation theory. *J. Geophys. Res.*, 91(B9):9239–9252.

Tversky, A. and Kahneman, D. (1974). Judgment under uncertainty: heuristics and biases. *ONR technical report*, (December).

Van der Wal, D., Chopra, P., Drury, M., and Gerald, J. F. (1993). Relationships between dynamically recrystallized grain size and deformation conditions in experimentally deformed olivine rocks. *Geophysical Research Letters*, 20(14):1479–1482.

Vaughan, P. J., Kohlstedt, D. L., and Waff, H. S. (1982). Distribution of the glass phase in hot-pressed, olivine-basalt aggregates: An electron microscopy study. *Contributions to Mineralogy and Petrology*, 81:253–261.

von Bargen, N. and Waff, H. S. (1986). Permeabilities, interfacial areas and curvatures of partially molten systems: Results of numerical computations of equilibrium microstructures. *Journal of Geophysical Research*, 91:9261.

2089 Vonlanthen, P. and Grobety, B. (2008). CSL grain boundary distribution in
2090 alumina and zirconia ceramics. *Ceramics International*, 34(6):1459–1472.

2091 Waff, H. S. and Bulau, J. R. (1979). Equilibrium fluid distribution in an ultramafic
2092 partial melt under hydrostratic stress conditions. *Journal of Geophysical*
2093 *Research*, 84(9).

2094 Wagner, J., Adjaoud, O., Marquardt, K., and Jahn, S. (2016). Anisotropy of
2095 self-diffusion in forsterite grain boundaries derived from molecular dynamics
2096 simulations. *Contributions to Mineralogy and Petrology*, 171:98.

2097 Walte, N., Rubie, D., Bons, P., and Frost, D. (2011). Deformation of a crystalline
2098 aggregate with a small percentage of high-dihedral-angle liquid: Implications
2099 for coremantle differentiation during planetary formation. *Earth and Planetary*
2100 *Science Letters*, 305(1-2):124–134.

2101 Walte, N. P., Bons, P. D., and Koehn, D. (2003). Disequilibrium melt distribution
2102 during static recrystallization. *Tectonophysics*, 31(11):1009–1012.

2103 Walte, N. P., Bons, P. D., and Passchier, C. W. (2005). Deformation of melt-
2104 bearing systemsinsight from in situ grain-scale analogue experiments. *Journal*
2105 *of Structural Geology*, 27(9):1666–1679.

2106 Wanamaker, B. J. and Kohlstedt, D. L. (1991). The effect of melt composition on
2107 the wetting angle between silicate melts and olivine. *Physics and Chemistry of*
2108 *Minerals*, 18(1):26–36.

2109 Watanabe, T. (1979). Misorientation dependence of grain boundary sliding in
2110 1010 tilt zinc bicrystals. *Philosophical magazine. A Physics of condensed matter,*
2111 *defects and mechanical properties [0141-8610]*, 40(5):667 –683.

2112 Watanabe, T. (1983). Observations of plane-matching grain boundaries by electron
2113 channelling patterns. *Philosophical magazine. A, Physics of condensed matter,*
2114 *defects and mechanical properties [0141-8610]*, 47(1):141 –146.

2115 Watanabe, T., Ara, K. I., Yoshim, K., and Oikawa, H. (1989). Texture and grain
2116 boundary character distribution (GBCD) in rapidly solidified and annealed Fe-
2117 6.5mass%Si ribbons. *Philosophical Magazine Letters*, 59(2):47–52.

Watson, G. W., Oliver, P. M., and Parker, S. C. (1997). Computer simulation of the structure and stability of forsterite surfaces. *Physics and Chemistry of Minerals*, 25(1):70–78.

Wenk, H.-R. (1985). *Preferred Orientation in Deformed Metal and Rocks: An introduction to Modern Texture Analysis*. ACADEMIC PRESS, INC.

White, J. C. and White, S. H. (1981). On the structure of grain boundaries in tectonites. *Tectonophysics*, 78(1-4):613–628.

Williams, D. B. and Carter, B. C. (2009). Transmission electron microscopy. *Book*.

Wirth, R. (1996). Thin amorphous films (1-2 nm) at olivine grain boundaries in mantle xenoliths from San Carlos, Arizona. *Contributions to Mineralogy and Petrology*, 124(1):44–54.

Witt-Eickschen, G. and O'Neill, H. S. C. (2005). The effect of temperature on the equilibrium distribution of trace elements between clinopyroxene, orthopyroxene, olivine and spinel in upper mantle peridotite. *Chemical Geology*, 221(1-2):65–101.

Yasuda, S., Yoshida, H., Yamamoto, T., and Sakuma, T. (2004). Improvement of High-temperature Creep Resistance in Polycrystalline Al2O3 by Cations Co-doping. *Materials Transactions*, 45(7):2078–2082.

Zaefferer, S. and Wright, S. I. (2009). *Electron Backscatter Diffraction in Materials Science*. Springer, New York, 2nd edition.

9 additional data

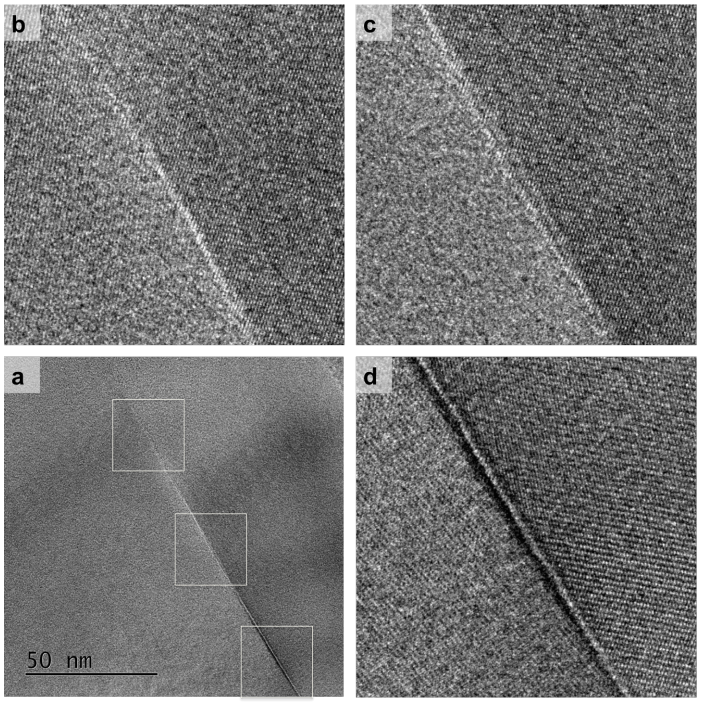

Fig. 18 Original HRTEM micrograph acquired without objective aperture. Same data as in Figure 6. In the latter it is displayed with frequencies only up to an equivalent d-spacing of 0.24 *nm* and background subtracted.